All-Optical Wavelength Conversion by Four-Wave Mixing in a Semiconductor Optical Amplifier

Thesis by

Robert Bumju Lee

In Partial Fulfillment of the Requirements

for the Degree of

Doctor of Philosophy

California Institute of Technology

Pasadena, California

1997

(Defended April 22, 1997)

To My Parents

Acknowledgments

First and foremost, I wish to express deepest thanks to my advisor, Professor Kerry J. Vahala. I have thoroughly enjoyed working with him and learning from him. His keen physical insight has continually provided invaluable guidance for this thesis. I will always appreciate the enthusiasm and patience with which he pursued any project.

I owe special thanks to David F. Geraghty, whom I have worked with closely for the past two years on the wavelength conversion experiments and to Dr. Charles S. Tsai with whom I collaborated on the GaAs selective epitaxy experiment. I would like to thank other members, present and past, in the Vahala group who have shared with me many stimulating discussions and have helped make my Ph.D. pursuit an enjoyable and rewarding experience: Guido Hunziker, Roberto Paiella, Renato Camata, Per Olof Hedekvist, Hunsuk Kim, Dr. Jianhui Zhou, Dr. Namkyoo Park, Dr. Jay W. Dawson, Dr. Winston Saunders, Dr. Pete Sercel, Dr. Steve Sanders and Dr. John Lebens. My appreciation also goes to Drs. Norman Kwong, Thomas Schrans and Al Benzoni of Ortel Corporation, Drs. James Singletery, Siamak Forouhar, Paul Maker and Rich Muller of the Jet Propulsion Laboratory, Dr. Tom Veegers of Northrop Grumman Corporation, and Dr. Gang He of Vitesse Corporation. The assistance of Rosalie Rowe on day to day matters is much appreciated.

The semiconductor optical amplifiers used in the experiments were supplied by Drs. Marc Verdiell, Mehrdad Ziari and Atul Mathur of SDL, Inc. Ortel Corporation has donated some of the DFB lasers and photodetectors used in the experiments

described in this thesis. In addition, the Advanced Research Projects Agency, the Office of Naval Research and the National Science Foundation provided funding for much of the research in this thesis.

Personally, I would like to acknowledge the National Defense Science and Engineering Graduate Fellowship for providing support for my graduate studies.

And finally, I would like to thank my parents and my sister for their unwavering support and patience throughout the years of my education. The culmination of the last five years in this thesis was made possible by their encouragement and understanding.

Abstract

Wavelength division multiplexed optical communication systems will soon become an integral part of commercial optical networks. A crucial new function required in WDM networks is wavelength conversion, the spectral translation of information-laden optical carriers, which enhances wavelength routing options and greatly improves network reconfigurability. One of several techniques for implementing this function is four-wave mixing utilizing ultra-fast intraband nonlinearities in semiconductor optical amplifiers.

The effects of input power, noise prefiltering and semiconductor optical amplifier length on the conversion efficiency and optical signal-to-noise ratio were examined. Systems experiments have been conducted in which several important performance characteristics of the wavelength converter were studied. A bit-error-rate performance of $< 10^{-9}$ at 10 Gb/s was achieved for a record shift of 18 nm down in wavelength and 10 nm up in wavelength. Two cascaded conversions spanning a 40 km fiber link at 10 Gb/s are also demonstrated for conversions of up to 9 nm down and up in wavelength. The dynamic range of input signal power and its impact on the BER performance were studied at 2.5 Gb/s for both a single-channel conversion and a simultaneous 2-channel conversion. The crosstalk penalty induced by parasitic cross-gain modulation in 2-channel conversion is quantified. The spectral inversion which results from the conversion process is studied by time-resolved spectral analysis, and its application as a technique for dispersion compensation is demonstrated.

Finally, the application of selective organometallic vapor-phase epitaxy for the

formation of highly-uniform and densely-packed arrays of GaAs quantum dots is demonstrated. GaAs dots of 15–20 nm in base diameter and 8–10 nm in height terminated by slow-growth crystallographic planes were grown within dielectric-mask openings and characterized by atomic force microscopy.

Contents

List of Figures

Chapter 1

Introduction

Semiconductor optical amplifiers are of increasing interest for applications in broadband lightwave communication systems such as wavelength conversion and ultrafast optical signal processing. In this thesis, broadband wavelength conversion by four-wave mixing (FWM) in a semiconductor optical amplifier (SOA) is studied for application in wavelength division multiplexed all-optical networks.

Chapter 2 is an introduction to four-wave mixing in a semiconductor optical amplifier. It contains an overview of both interband and intraband carrier dynamics in an SOA and how they contribute to the four-wave mixing process. A simple theory governing the nonlinear process is presented. FWM is found to be an effective analysis tool for studying the ultra-fast intraband dynamics of a semiconductor optical amplifier.

Chapter 3 first presents an introduction to all-optical networks and the potential role and benefit of wavelength conversion. The several conditions for optimizing the wavelength converter performance based on FWM in an SOA are examined. The

conversion efficiency and optical signal-to-noise ratio as a function of input power and ASE prefiltering are characterized and significant improvements are predicted by increasing the length of the semiconductor optical amplifier. The SOAs used in this thesis research are InGaAs/InGaAsP strained multiple quantum well traveling-wave amplifiers operating at 1.55 μm.

Chapters 4–7 describe system experiments conducted using a wavelength converter based on FWM in an SOA. Chapter 4 describes a wavelength conversion experiment in which bit-error-rate (BER) measurements are performed on the converted signal. The spectral range over which satisfactory BER performance is achieved ($< 10^{-9}$) at 10 Gb/s is characterized.

Chapter 5 describes a cascaded wavelength conversion experiment. Cascadability is essential to practical implementation of any wavelength conversion technique. We demonstrate a transmission link of two cascaded conversions spanning 40 km of single-mode fiber at 10 Gb/s for up to 9 nm of wavelength shift.

Chapter 6 describes a simultaneous 2-channel conversion experiment. The dynamic range of the input signal is characterized in a single-channel conversion. The results are compared to a similar experiment in the case of 2-channel conversion and the crosstalk penalty is quantified at 2.5 Gb/s.

Chapter 7 describes an application of the spectral inversion which results from the four-wave mixing wavelength conversion process toward dispersion compensation. The spectral inversion between the input and the converted signal is measured by a time-resolved spectral analysis experiment. Dispersion compensation by mid-span

spectral inversion demonstrates how the adverse effects of chromatic dispersion in dispersive single-mode fiber on a chirped signal source can be overcome.

Finally, Chapter 8 presents an experiment on the formation of highly-uniform and densely-packed arrays of GaAs quantum dots by selective epitaxy. GaAs dots of 15–20 nm in base diameter and 8–10 nm in height terminated by slow-growth crystallographic planes were grown within dielectric-mask openings by Chloride-based selective organometallic vapor-phase epitaxy. The dots are characterized by contact-mode atomic force microscopy.

In Appendix A, an optically preamplified receiver is described in context of bit-error-rate measurements on the small optical powers of the wavelength converted signal. The measured characteristics of the low-noise optical preamplifier used in the experiment is presented qualifying the spectral dependence of the BER measurements presented in Chapters 4–7.

Work presented here is contained in the following published articles and conference proceedings [1]–[14].

Bibliography

[1] Charles S. Tsai, Robert B. Lee and Kerry J. Vahala, "Formation of highly-uniform and densely-packed arrays of GaAs dots by selective epitaxy," Materials Research Society Proceedings vol. 358, *Microcrystalline and Nanocrystalline Semiconductors*, pp. 969–974, 1994.

[2] H. A. Atwater, K. J. Vahala, R. C. Flagan, R. Camata, R. B. Lee, K. V. Shcheglov, C. S. Tsai and C. M. Yang, "Group III-V and group IV quantum dot synthesis," *Low Dimensional Structures prepared by Epitaxial Growth or Regrowth on Patterned Substrates*, pp. 69–80, 1995.

[3] Kerry J. Vahala, Jianhui Zhou, David Geraghty, Robert Lee, Mike Newkirk and Barry Miller, "Four-wave mixing in semiconductor traveling-wave amplifiers for wavelength conversion in all-optical networks," *International Journal of High Speed Electronics & Systems*, vol. 7, pp. 153–177, 1996.

[4] David F. Geraghty, Robert B. Lee, Kerry J. Vahala, Marc Verdiell, Mehrdad Ziari and Atul Mathur, "Wavelength conversions up to 18 nm at 10 Gb/s by four-wave mixing in a semiconductor optical amplifier," *IEEE Photon. Technol. Lett.*, vol. 9, pp. 452-454, 1997.

[5] Robert B. Lee, David F. Geraghty, Kerry J. Vahala, Marc Verdiell, Mehrdad Ziari and Atul Mathur, "Cascaded wavelength conversion by four-wave mixing in a strained semiconductor optical amplifier at 10 Gb/s," *IEEE Photon. Technol. Lett.*, vol. 9, June, 1997.

[6] David F. Geraghty, Robert B. Lee and Kerry J. Vahala, "Cascaded wavelength conversions by four-wave mixing in semiconductor optical amplifiers at 10 Gb/s," *OSA Trends in Optics and Photonics Series, Systems Technologies*, vol. 12, 1997.

[7] Kerry Vahala, Jianhui Zhou, David Geraghty, Robert Lee, Michael Newkirk and Barry Miller, "Wavelength shifting by four-wave mixing in semiconductor optical amplifiers," *IEEE Laser and Electro-Optics Society 1995 Annual Meeting*, San Francisco, California, October 30–November2, 1995, paper OC4.2. (Invited)

[8] K. J. Vahala, D. Geraghty, R. B. Lee, J. Zhou, M. A. Newkirk and B. I. Miller, "Application of terahertz dynamics in semiconductor optical amplifiers to wavelength conversion in WDM systems," SPIE Proceedings vol. 2684, *High-Speed Semiconductor Laser Sources*, San Jose, California, January 27–February 2, 1996, paper 2684-01. (Invited)

[9] Kerry Vahala, Robert Lee, David Geraghty, Per Olof Hedekvist and Jianhui Zhou, "Four-wave mixing in semiconductor optical amplifiers for application to ultra-fast wavelength conversion," *1st Optoelectronics and Communications Conference*, Chiba, Japan, July 16–19, 1996, paper 18D2-1. (Invited)

[10] Kerry J. Vahala, Robert B. Lee, David F. Geraghty, Guido Hunziker and Roberto Paiella, "Wavelength conversion by four-wave mixing in semiconductor amplifiers," *Optical Society of America 1996 Annual Meeting*, Rochester, New York, October 20–24, 1996, paper MDD2. (Invited)

[11] Robert B. Lee, David F. Geraghty, Per Olof Hedekvist and Kerry J. Vahala, "Crosstalk penalty in 2-channel wavelength conversion by four-wave mixing in a strained semiconductor optical amplifier," *Optical Fiber Communication Conference 1997*, Dallas, Texas, February 16–21, 1997, poster WL53.

[12] David F. Geraghty, Robert B. Lee and Kerry J. Vahala, "Cascaded wavelength conversions using four-wave mixing in semiconductor optical amplifiers," *Optical Fiber Communication Conference 1997*, Dallas, Texas, February 16–21, 1997, paper WH6.

[13] Kerry Vahala, Roberto Paiella, Guido Hunziker, Robert Lee and David Geraghty, "Ultrafast semiconductor carrier dynamics probed by four-wave mixing and application to all-optical signal processing in WDM systems," *Optical Society of*

America 1997 Ultrafast Electronics and Optoelectronics Topical Meeting, Lake Tahoe, Nevada, March 17–19, 1997, paper UMC1. (Invited)

[14] David F. Geraghty, Robert B. Lee and Kerry J. Vahala, "Time-resolved spectral analysis of phase conjugation by four-wave mixing in a semiconductor optical amplifier," *Conference on Lasers and Electro-Optics 1997*, Baltimore, Maryland, May 18–23, 1997, paper CTuH.

Chapter 2

Four-Wave Mixing in a Semiconductor Optical Amplifier

2.1 Introduction

The first semiconductor lasers were demonstrated in 1962 by four research groups [1]–[4]. These devices based on GaAs operated in pulsed mode at 0.88 μm. Semiconductor lasers developed slowly in the early stages, however, significant strides have been made in more recent years. In the 1980's, semiconductor lasers assumed paramount importance through their presence in consumer products like the compact disc players and the laser printers. In 1979 silica fibers exhibiting low dispersion and low loss in the wavelength regions near 1.3 μm and 1.55 μm, respectively, had been developed [5]. The development of semiconductor lasers operating at these wavelengths using InGaAsP/InP material system were motivated by the need for compact and low-power consuming optical signal sources. The sophisticated structures required in

demanding applications such as high-speed lightwave communication systems were facilitated by the development of epitaxial techniques like molecular-beam epitaxy and organometallic vapor-phase epitaxy which became available in the 1980's. Today, semiconductor lasers with a modulation bandwidth of 30 GHz [6] and uncooled cw operation at 170°C [7] have been demonstrated.

Research on semiconductor optical amplifiers (SOAs) started soon after the invention of semiconductor lasers [8][9]. SOAs are typically classified into two groups: Fabry-Perot amplifier and traveling-wave amplifier. All lasers act as Fabry-Perot amplifiers close to but before reaching lasing threshold. Due to the Fabry-Perot cavity formed through the reflections at the facets, the gain G_{FP} is enhanced when the frequency is resonant with the cavity, and thus the gain bandwidth is determined by the bandwidth of this resonance. Ideal optical amplifiers without any feedback from the facets are called traveling-wave amplifiers. For practical purposes, an SOA may be called a traveling-wave amplifier if the gain ripple, *i.e.*, the ratio of the maximum to minimum value of G_{FP} does not exceed 3 dB. For this condition to be satisfied for an amplifier with 30 dB gain, the required facet reflectivity is $< 1.7 \times 10^{-4}$. These reflectivities can only be achieved with considerable effort. Several techniques have been demonstrated including multi-layer anti-reflection coating [10], angled-facet or tilted-stripe structures [11][12], and buried-facet or window-facet structures [13].

In a high bit-rate, loss-limited fiber-optic communication system, periodic optical amplification is a simpler and less expensive solution than using optoelectronic repeaters [14]. Although SOAs have been used as in-line amplifiers [15], Erbium-

doped fiber amplifiers (EDFAs) are the preferred choice in long-haul dispersion shifted fiber [16] or dispersion managed fiber-optic links [17]. However, due to the small size and the electrical pumping properties, SOAs remain attractive for many applications involving optoelectronic integration such as photonic switching, optical interconnects, and photonic integrated circuits for optical transmitters and receivers [18][19].

In this chapter, basic carrier dynamics of semiconductor optical amplifers with characteristic time constants ranging from 100 fs to 1 ns are reviewed. The basic physics of four-wave mixing in SOAs is also discussed, which provides an effective frequency-domain technique to probe the ultra-fast intraband semiconductor dynamics.

2.2 Semiconductor Carrier Dynamics

The most important property of a semiconductor optical amplifier is gain and its saturation behavior. If we consider a cw input beam whose wavelength nearly coincides with the gain peak, in most cases of interest, the gain per unit length can be assumed to increase linearly with the carrier density N as [20]

$$g(N) = a(N - N_0), \tag{2.1}$$

where a is the differential gain coefficient and N_0 is the carrier density in the SOA active region when transparency is reached. The carrier density N in the presence of an injection current I and optical signal power P changes according to a carrier-rate

equation as

$$\frac{dN}{dt} = \frac{I}{qV} - \frac{N}{\tau_s} - \frac{g(N)}{A\hbar\omega}P, \tag{2.2}$$

where q is the electron charge, V is the active region volume, τ_s is the spontaneous carrier lifetime and A is the cross-section area of the waveguide mode. For times much longer than τ_s, a steady-state solution for N can be substituted into Eqn. 2.1, and the optical gain saturates according to

$$g(N) = \frac{a(I\tau_s/qV - N_0)}{1 + P/P_s} = \frac{g_0}{1 + P/P_s}, \tag{2.3}$$

where the saturation power P_s is given by

$$P_s = \frac{A\hbar\omega}{a\tau_s} \tag{2.4}$$

and where $g_0 = a(I\tau_s/qV - N_0)$ is the unsaturated small-signal gain coefficient.

The gain saturation by carrier depletion through stimulated emission represents only the slowest dynamics in an SOA. In Fig. 2.1 are summarized the timescales associated with the different physical processes. If an impulse of occupancy at a given localized energy is generated at time $t = 0$ in a given band of a semiconductor, the carrier occupancy equilibrates to a quasi-Fermi distribution by Coulomb scattering with a characteristic time constant $\tau_1 \sim 100$ fs. The carrier temperature, however, is greater than that of the lattice. On a timescale of $\tau_h \sim 1$ ps, by emission or absorption of phonons, the carrier distribution relaxes to that of the lattice temperature. And finally the carrier density relaxes by interband electron-hole recombination with a characteristic timescale determined by the stimulated emission lifetime $\tau_s \sim 200$ ps.

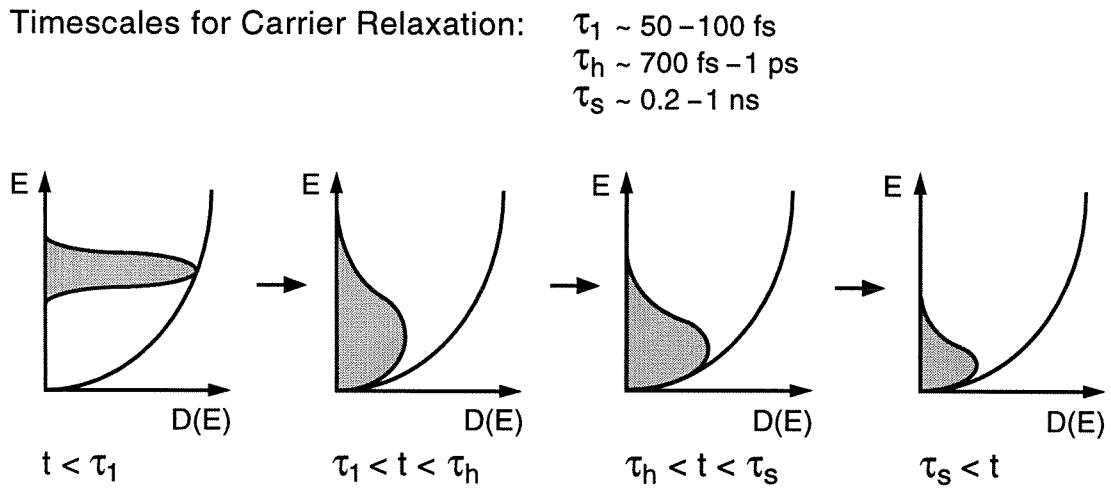

Figure 2.1: An illustration of the important timescales for carrier relaxation in a semiconductor optical amplifer.

Thus, in addition to interband gain saturation, there are gain nonlinearities associated with the intraband processes with time constants τ_1 and τ_h, typically referred to as spectral hole burning and dynamic carrier heating, respectively. These processes are intrinsically weak, however, they are essential in realizing useful nonlinear functionalities like wavelength conversion [21][22].

2.3 Terahertz Four-Wave Mixing Spectroscopy

Nondegenerate four-wave mixing (FWM) in semiconductor optical amplifiers has been a topic of increasing interest over the past several years. A schematic illustrating the experimental configuration is shown in Fig. 2.2. Two optical waves, pump (p) and signal (s), whose fields are labeled E_p and E_s, are input to the SOA. The choice for the

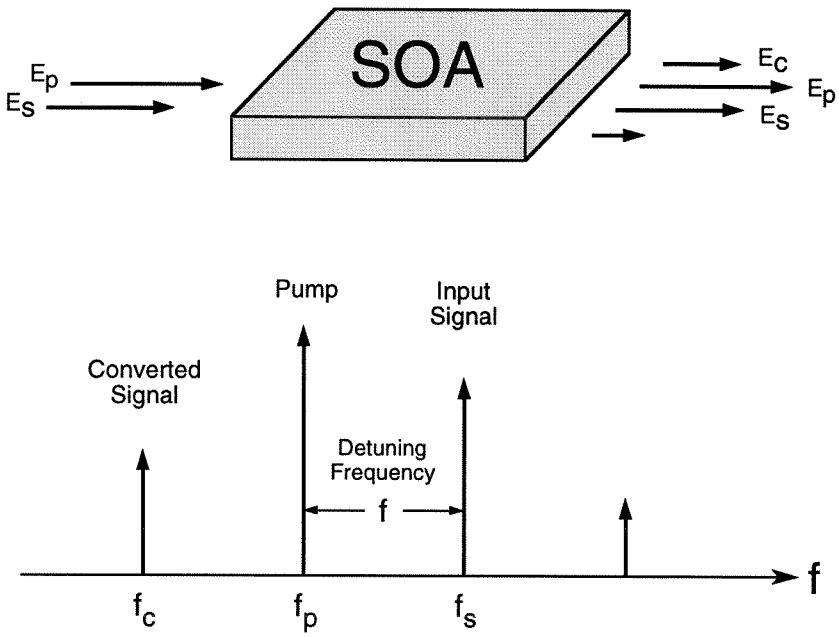

Figure 2.2: Schematic illustration of the four-wave mixing configuration and the resulting spectrum at the output of the semiconductor optical amplifier.

labeling is made in reference to application of FWM toward wavelength conversion. The detuning frequency f of the input waves is given by $f = f_s - f_p$. At the output of the SOA, are two additional waves. The converted signal wave at frequency $f_c = 2f_p - f_s$ is generated by the scattering of the pump wave off a grating established in the SOA in response to the beating of the pump and the signal wave. When the role of the pump and the signal are reversed, the identical scattering process generates the fourth wave shown.

The physical processes discussed in the previous section are responsible for the dynamic index and gain gratings established in the SOA. The strength of the grat-

ing and therefore the efficiency with which the converted signal can be generated as a function of detuning frequency, depends on the relative strengths of the nonlinearities and the respective time constants for the different physical processes. The idea of carrier density modulation and spectral hole burning resulting in nondegenerate four-wave mixing in an SOA was first investigated theoretically by Agrawal based on a density-matrix formalism [23]. It was not realized experimentally until the work of Tiemeijer [24] and later Kikuchi *et al.* [25] and Zhou *et al.* [26]–[28]. The first experiment with detuning frequencies in excess of 1 THz was demonstrated by Zhou *et al.* [27]. Nondegenerate FWM has also been demonstrated in semiconductor lasers [29][30].

A comprehensive theoretical overview can be found in References [31] and [32]. In this section, a set of simple coupled equations and a highly abbreviated form for the third order nonlinearities are used to describe the field evolution of the converted signal in the SOA. Assume the following form for the guided waves of the copolarized pump, signal and converted waves,

$$\mathcal{E}_j(z,t) = E_j(z)\exp[i(k_j z - \omega_j t)] \tag{2.5}$$

where $j = p, s, c$ denote the pump, signal and the converted wave, respectively; and $\{E_j(z)\}$ are the slowly-varying amplitudes of the three waves. Using procedures similar to those of Agrawal [23] results in the following set of coupled equations

$$\frac{dE_{p,s}(z)}{dz} = \frac{1}{2}\left[\frac{g_0}{1+\frac{P(z)}{P_s}}(1-i\alpha)-\alpha_l\right]E_{p,s}(z) \tag{2.6}$$

$$\frac{dE_c(z)}{dz} = \frac{1}{2}\left[\frac{g_0}{1+\frac{P(z)}{P_s}}(1-i\alpha)-\alpha_l\right]E_c(z) - \kappa(z)\,E_p^2(z)\,E_s^*(z)\exp(i\Delta kz) \tag{2.7}$$

where $P(z)$ is the total power in the SOA, α is the linewidth enhancement factor, α_l is the internal loss of the SOA per unit length and $\Delta k = 2k_p - k_s - k_c$ is the phase mismatch. The phase mismatch, however, can be neglected even for detunings greater than 1 THz and a device length of 1 mm according to the measured value of the group index dispersion [33]. Eqn. 2.6 simply describes the amplification of the pump and the signal waves neglecting any power depletion of the pump due to FWM. Due to the small conversion efficiencies, for detunings greater than a few tens of GHz, the power in the converted wave can be neglected in $P(z)$. For the converted wave, the first term of Eqn. 2.7 again simply describes amplification and the second term describes the generation of the converted wave by FWM proportional to the phase conjugate of the signal wave. The coupling coefficient $\kappa(z)$ measures the strength of the nonlinear mixing process and has the form

$$\kappa(z) = \frac{1}{2}\,\frac{g_0}{1+\frac{P(z)}{P_s}}\sum_{m=1}^{3}\frac{1-i\alpha_m}{P_m}\,\frac{1}{1-i2\pi f\tau_m}. \tag{2.8}$$

The indices $m = 1, 2, 3$ are for carrier density modulation, dynamic carrier heating and spectral hole burning, respectively. For each of the mechanisms, $\{\alpha_m\}$ are the ratio between the real and the imaginary parts of the induced refractive index change, and $\{P_m\}$ and $\{\tau_m\}$ are the saturation powers and time constants.

In the small-signal regime in which the saturation effects can be neglected, the

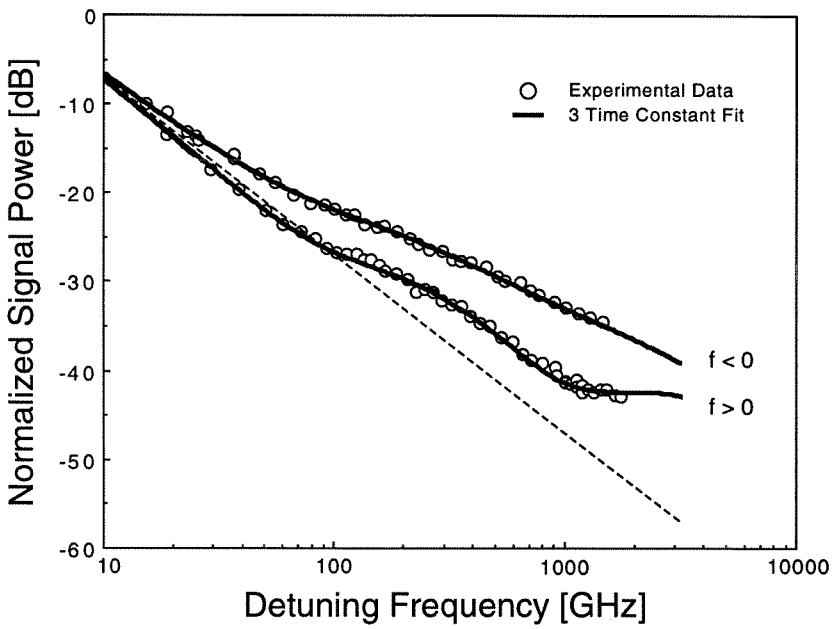

Figure 2.3: The normalized four-wave mixing converted signal power vs. positive and negative pump-signal detuning frequency and the theoretical fits according to Eqn. 2.9. A 20 dB/dec reference is shown as a dashed line. (Ref. [27])

converted signal power P_c can be approximated by [27]

$$P_c = P_p^2 P_s \left| \sum_{m=1}^{3} \frac{C_m}{1 - i2\pi f \tau_m} \right|^2 \tag{2.9}$$

where P_p and P_s are pump and signal powers at the SOA output and $\{C_m\}$ are complex coupling coefficients. The experimentally measured converted signal power by high-sensitivity heterodyne detection can be fitted according to Eqn. 2.9. By simultaneously fitting the data for both positive and negative detunings, one can determine the relative strengths and the characteristic time constants of the different mechanisms.

In Fig. 2.3 is shown the normalized converted signal power vs. detuning frequencies from -1.5 THz to 1.7 THz for a tensile-strained SOA biased at 100 mA [27]. The fits according to Eqn. 2.9 are in excellent agreement with the data. The time constants are $\tau_1 = 200$ ps, $\tau_2 = 650$ fs and $\tau_3 = 50$ fs. The significant asymmetry in the conversion efficiency for positive and negative detunings is attributed to the phase interferences which occur among the various contributing mechanisms.

The parameters are consistent with the time-domain pump-probe measurements using ultra-short optical pulses by Hall *et al.* [34][35]. Thus Terahertz four-wave mixing spectroscopy has proven itself to be an effective complimentary technique to time-domain measurements for probing the ultra-fast dynamics in a semiconductor optical amplifier. In recent months, four-wave mixing spectroscopy has further been demonstrated as an effective tool for studying the inter-well carrier transport in multi-quantum well active regions of a semiconductor optical amplifier [36][37].

Bibliography

[1] R. N. Hall, G. E. Fenner, J. D. Kingley, T. J. Soltys and R. O. Carlson, "Coherent light emission from GaAs junctions," *Phys. Rev. Lett.*, vol. 9, pp. 366–368, 1962.

[2] M. I. Nathan, W. P. Dumke, G. Burns, F. H. Dill, Jr. and G. Laser, "Stimulated emission of radiation from GaAs p-n junctions," *Appl. Phys. Lett.*, vol. 1, pp. 62–64, 1962.

[3] N. Holonyak, Jr. and S. F. Bevacqua, "Coherent (visible) light emission from $Ga(As_{1-x}P_x)$ junctions," *Appl. Phys. Lett.*, vol. 1, pp. 82–83, 1962.

[4] T. M. Quist, R. H. Rediker, R. J. Keyes, W. E. Krag, B. Lax, A. L. McWhorter and H. J. Zieger, "Semiconductor maser of GaAs," *Appl. Phys. Lett.*, vol. 1, pp. 91–92, 1962.

[5] T. Miya, Y. Terunuma, T. Hosaka and T. Miyashita, "Ultimate low-loss single-mode fibre at 1.55 μm," *Electron. Lett.*, vol. 15, pp. 106–108, 1979.

[6] Y. Matsui, H. Murai, S. Arahira, S. Kutsuzawa and Y. Ogawa, "30-GHz bandwidth 1.55 μm strain-compensated InGaAlAs-InGaAsP MQW laser," *IEEE Photon. Technol. Lett.*, vol. 9, pp. 25–27, 1997.

[7] M. C. Wang, W. Lin, T. T. Shi and Y. K. Tu, "Ultrahigh temperature and ultrahigh-speed operation of 1.3 μm strain-compensated AlGaInAs/InP uncooled laser-diodes," *Electron. Lett.*, vol. 31, pp. 1584–1585, 1995.

[8] J. W. Crowe and R. M. Craig, Jr., "Small-signal amplification in GaAs lasers," *Appl. Phys. Lett.*, vol. 4, pp. 57–58, 1964.

[9] W. F. Kosonocky and R. H. Cornely, "GaAs laser amplifiers," *IEEE J. Quantum Electron.*, vol. QE-4, pp. 125–131, 1968.

[10] T. Saitoh, T. Mukai and O. Mikami, "Theoretical-analysis and fabrication of antireflection coatings on laser-diode facets," *J. Lightwave Technol.*, vol. 3, pp. 288–293, 1985.

[11] C. E. Zah, J. S. Osinski, C. Caneau, S. G. Menocal, L. A. Reith, J. Salzman, F. K. Shokoohi and T. P. Lee, "Fabrication and performance of 1.5 μm GaInAsP traveling-wave laser-amplifiers with angled facets," *Electron. Lett.*, vol. 23, pp. 990–992, 1987.

[12] A. J. Collar, G. D. Henshall, J. Farre, B. Mikkelsen, Z. Wang, L. Eskildsen, D. S. Olesen and K. E. Stubkjaer, "Low residual reflectivity of angled-facet semiconductor-laser amplifiers," *IEEE Photon. Technol. Lett.*, vol. 2, pp. 553–555, 1990.

[13] N. A. Olsson, R. G. Kazarinov, W. A. Nordland, C. H. Henry, M. G. Oberg, H. G. White, P. A. Garbinski and A. Savage, "Polarization-independent optical amplifier with buried facets," *Electron. Lett.*, vol. 25, pp. 1048–1049, 1989.

[14] G. P. Agrawal, *Fiber-Optic Communication Systems*, J. Wiley & Sons, New York, 1992.

[15] M. G. Oberg, N. A. Olsson, L. A. Koszi and G. J. Przybylek, "313-km transmission experiment at 1 Gbit/s using optical amplifiers and a low chirp laser," *Electron. Lett.*, vol. 24, pp. 38–39, 1988.

[16] H. Taga, M. Suzuki, Y. Yoshida, S. Yamamoto and H. Wakabayashi, "Bit-error-rate characterization of IM-DD ultralong-distance optical communication-systems with Er-doped fiber amplifiers using a recirculating loop," *J. Lightwave Technol.*, vol. 11, pp. 2100–2104, 1993.

[17] D. Garthe, W. S. Lee, R. A. Saunders, B. L. Paten and A. Hadjifotiou, "Demonstration of 80 Gbit/s WDM transmission over 537 km of nonzero dispersion shifted fiber without in-line dispersion management or gain equalization," *Electron. Lett.*, vol. 32, pp. 1217–1218, 1996.

[18] Special Issue on Optical Amplifiers, *J. Lightwave Technol.*, vol. 9, February 1991.

[19] Special Issue on Photonic Integrated Circuits, *Opt. and Photon. News*, vol. 4, March 1993.

[20] G. P. Agrawal and N. K. Dutta, *Semiconductor Lasers*, 2nd ed., Van Nostrand Reinhold, New York, 1993.

[21] M. C. Tatham, G. Sherlock and L. D. Westbrook, "20 nm wavelength conversion using nondegenerate four-wave mixing," *IEEE Photon. Technol. Lett.*, vol. 5, pp. 1303–1306, 1993.

[22] J. Zhou, N. Park, K. J. Vahala, M. A. Newkirk and B. I. Miller, "Four-wave mixing wavelength conversion efficiency in semiconductor traveling-wave amplifiers measured to 65 nm of wavelength shift," *IEEE Photon. Technol. Lett.*, vol. 6, pp. 984–987, 1994.

[23] G. P. Agrawal, "Population pulsations and nondegenerate four-wave mixing in semiconductor lasers and amplifiers," *J. Opt. Soc. Am. B*, vol. 5, pp. 147–158, 1988.

[24] L. F. Tiemeijer, "Effects of nonlinear gain on four-wave mixing and asymmetric gain saturation in a semiconductor laser amplifier," *Appl. Phys. Lett.*, vol. 59, pp. 499–501, 1991.

[25] K. Kikuchi, M. Kakui, C. E. Zah and T. P. Lee, "Observation of highly nondegenerate four-wave mixing in a 1.5 μm traveling-wave semiconductor optical amplifier and estimation of nonlinear gain coefficient," *IEEE J. Quantum Electron.*, vol. QE-28, pp. 151–156, 1992.

[26] J. Zhou, N. Park, J. W. Dawson, K. J. Vahala, M. A. Newkirk, U. Koren and B. I. Miller, "Highly nondegenerate four-wave mixing and gain nonlinearity in a strained multiple-quantum-well optical amplifier," *Appl. Phys. Lett.*, vol. 62, pp. 2301–2303, 1993.

[27] J. Zhou, N. Park, J. W. Dawson, K. J. Vahala, M. A. Newkirk and B. I. Miller, "Terahertz four-wave mixing spectroscopy for study of ultrafast dynamics in a semiconductor optical amplifier," *Appl. Phys. Lett.*, vol. 63, pp. 1179–1181, 1993.

[28] J. Zhou, N. Park, J. W. Dawson, K. J. Vahala, M. A. Newkirk and B. I. Miller, "Efficiency of broadband four-wave mixing wavelength conversion using semiconductor traveling-wave amplifiers," *IEEE Photon. Technol. Lett.*, vol. 6, pp. 50–52, 1994.

[29] S. Murata, A. Tomita, J. Shimizu, M. Kitamura and A. Suzuki, "Observation of highly nondegenerate four-wave mixing (> 1 THz) in an InGaAsP multiple quantum-well laser," *Appl. Phys. Lett.*, vol. 58, pp. 1458–1460, 1991.

[30] S. Jiang and M. Dagenais, "Observation of nearly degenerate and cavity-enhanced highly nondegenerate four-wave mixing in semiconductor lasers," *Appl. Phys. Lett.*, vol. 62, pp. 2757–2759, 1993.

[31] A. Uskov, J. Mørk and J. Mark, "Wave mixing in semiconductor laser amplifiers due to carrier heating and spectral hole burning," *IEEE J. Quantum Electron.*, vol. QE-30, pp. 1769–1781, 1994.

[32] A. Mecozzi, S. Scotti, A. Dottavi, E. Iannone and P. Spano, "Four-wave-mixing in traveling-wave semiconductor amplifiers," *IEEE J. Quantum Electron.*, vol. QE-31, pp. 689–699, 1995.

[33] K. L. Hall, G. Lenz and E. P. Ippen, "Femtosecond time domain measurements of group velocity dispersion in diode lasers at 1.5 μm," *J. Lightwave Technol.*, vol. 10, pp. 616–619, 1992.

[34] K. L. Hall, J. Mark, E. P. Ippen and G. Eisenstein, "Femtosecond gain dynamics in InGaAsP optical amplifiers," *Appl. Phys. Lett.*, vol. 56, pp. 1740–1742, 1990.

[35] K. L. Hall, G. Lenz, E. P. Ippen, U. Koren and G. Raybon, "Carrier heating and spectral hole burning in strained-layer quantum-well laser amplifiers at 1.5 μm," *Appl. Phys. Lett.*, vol. 61, pp. 2512–2514, 1992.

[36] J. Zhou, N. Park, K. J. Vahala, M. A. Newkirk and B. I. Miller, "Study of inter-well carrier transport by terahertz four-wave mixing in an optical amplifier with tensile and compressively strained quantum wells," *Appl. Phys. Lett.*, vol. 65, pp. 1897–1899, 1994.

[37] R. Paiella, G. Hunziker, K. J. Vahala and U. Koren, "Measurement of the interwell carrier transport lifetime in multi-quantum-well optical amplifiers by polarization-resolved four-wave mixing," *Appl. Phys. Lett.*, vol. 69, pp. 4142–4144, 1996.

Chapter 3

All-Optical Networks and Wavelength Conversion by Four-Wave Mixing

The expansion of wide-area networks consisting of high-speed all-optical transmission links is driven by the rapidly increasing demand for large bandwidth applications like the World Wide Web in addition to telecommunications. The demand for bandwidth results not only from the increasing number of users, but more importantly from the bandwidth demand per user. Until recently, the high data-rate all-optical links have been based on a point-to-point architecture. However, to accommodate the ever increasing traffic, one needs a sophisticated scalable network consisting of optical cross-connects with active network management functionalities. Wavelength division multiplexing (WDM) together with wavelength conversion, *i.e.*, the spectral

translation of information-laden optical carriers, is a well-suited architecture for this purpose [1][2].

In this chapter, a general overview of the potential role of wavelength conversion in a WDM network and its benefits are presented. Then, we examine in detail a particular wavelength conversion technique based on four-wave mixing in a semiconductor optical amplifier. Practical issues regarding its application are studied. A simple model is used to assess how input power and ASE prefiltering affect the fidelity of the resulting wavelength converted signal, and improved converter performance is predicted for a converter based on a longer semiconductor optical amplifier.

3.1 Wavelength Conversion in a WDM Network

State-of-the-art commercial terrestrial telecommunication systems operate at 10 Gb/s. The new transoceanic links (Trans-Pacific Cable TPC-5) operate at 5 Gb/s and recent field tests have demonstrated up to 25 Gb/s operation [3]. However, to access the potential for more than 1 Tb/s capacity in the 1.5 μm low-loss window in silica fiber, simply increasing the single-channel data-rate is insufficient. A very effective utilization of the fiber bandwidth can be made in the wavelength domain rather than in the time domain in which multiple optical carriers at different wavelengths (wavelength division multiplexing) are launched simultaneously on to a single fiber therby increasing the aggregate capacity of a given link. In addition, wavelength can be used to perform routing and switching functions. Key component technologies for establishing such a network include passive splitters, space switches and wavelength

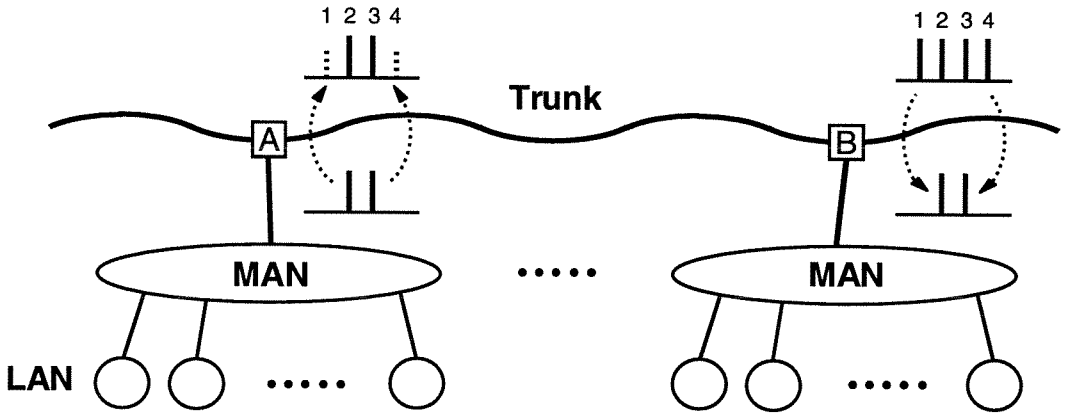

Figure 3.1: Highly simplified architecture for global optical network showing three layers. Wavelength converters improve wavelength routing flexibility and ease of scheduling access.

multiplexers/demultiplexers [4]–[6]. These components are becoming commercially available for large-scale deployment.

In the past several years, there has been a growing concensus toward the use of WDM in future networks. In 1996 three groups from Fujitsu, Lucent and NTT demonstrated in the laboratory 1 Tb/s transmission using 10–55 wavelengths with single-channel bit-rates ranging from 20 to 100 Gb/s [7]–[9]. In 1997 MCI has conducted field tests in their existing terrestrial system over a route of 443 km using four wavelengths at 10 Gb/s each [10].

In a WDM network, wavelength conversion serves a crucial function as illustrated in Fig. 3.1. Suppose that in transmitting information on wavelengths λ_2 and λ_3 from the metropolitan area network (MAN) on the left, one finds those wavelengths to be in use on the trunk line at node A. With wavelength conversion, the information

can be transferred to λ_1 and λ_4 and transmitted to the second MAN at node B at which point the wavelengths can again be converted back to λ_2 and λ_3. This simple illustration shows how wavelength conversion makes possible efficient reuse of wavelengths, resolves possible wavelength contention and allows for distributed network management based on local information. When the optical path involves multiple such nodes, the effectiveness of wavelength conversion can be measured by the improvements predicted in the throughput and network utilization by decreasing the blocking probability [11][12].

There are many possible ways to accomplish the wavelength conversion function as described in a recent review article [13]. The simplest approach is optoelectronic signal regeneration, *i.e.*, signal detection and subsequent modulation of a source at the new desired wavelength. However, with optical amplifiers replacing regenerators already in place, most network operators hope to avoid regeneration. The remaining techniques are all-optical.

In a semiconductor optical amplifier, the amplifier gain can be modulated with an input signal, thus encoding this gain modulation on a cw probe traveling through the SOA at another wavelength [14][15]. The cross-gain modulation technique generates a converted signal which is inverted in its intensity pattern. By incorporating SOAs in both arms of a Mach-Zehnder interferometer and injecting an input signal through one of the arms, the phase modulation associated with gain saturation in one arm is converted to an amplitude modulation by the interferometer [16]. Cross-phase modulation allows for high contrast modulation at the new wavelength. These two

techniques, however, are limited to ASK (amplitude-shift key) modulation format and bit-rates limited by the stimulated recombination lifetime.

Techniques based on nonlinear wave mixing, however, generate a converted signal in which both the phase and amplitude information are preserved offering strict transparency to the modulation format. Difference-frequency generation (DFG) using $\chi^{(2)}$ nonlinearities in passive quasi-phase-matched $LiNbO_3$ or AlGaAs waveguides has been demonstrated [17][18]. Also, four-wave mixing in both semiconductor optical amplifiers [19][20] and in silica fiber [21] has been used for wavelength conversion. However, due to the long interaction lengths (> 1 km) necessary, FWM in dispersion-shifted fiber is limited in its wavelength of operation to near the dispersion-zero wavelength to minimize phase mismatch.

The techniques mentioned above have advantages and disadvantages in terms of their intrinsic properties and maturity of the technology. The advantages of FWM in an SOA include flexible tunability of the input and output wavelengths within the gain bandwidth of the SOA, multi-channel operation, possibility of monolithic integration and transparency to both the bit-rate and the modulation format.

3.2 Wavelength Conversion by Four-Wave Mixing in a Semiconductor Optical Amplifier

In this section and in Chapters 4–7, the performance of wavelength converter based on four-wave mixing in a semiconductor optical amplifier is studied in detail.

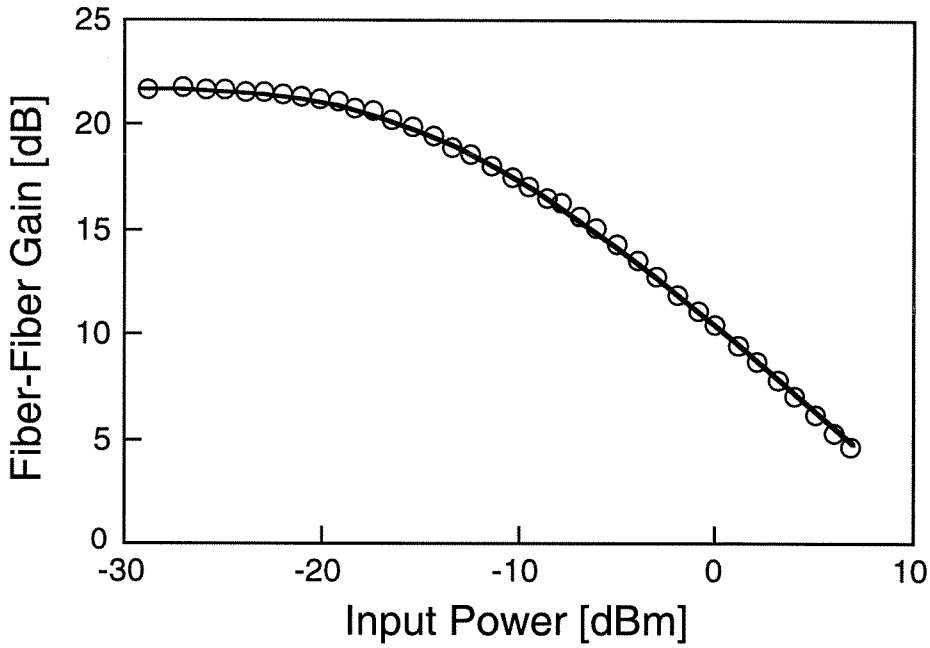

Figure 3.2: Measured fiber-to-fiber gain at 1550 nm of a compressively-strained semiconductor optical amplifer at 300 mA bias current, and a theoretical fit according to Eqn. 3.1.

3.2.1 Semiconductor Optical Amplifier Characteristics

The semiconductor optical amplifier used in this study is a compressively-strained multiple quantum well amplifier 1 mm in length with straight anti-reflection coated facets made by SDL, Inc. The device is fiber-pigtailed to single-mode fiber in a 14-pin butterfly package. For all experiments, the temperature is stabilized to approximately 25°C.

The most important parameter characterizing an SOA is gain and its saturation behavior. The fiber-to-fiber gain along the TE polarization, (gain for the TM polarization is negligible for a compressively-strained quantum well) is measured at

1550 nm near the gain peak for input powers ranging over 30 dB. The unsaturated small-signal fiber-to-fiber gain is approximately 22 dB as shown in Fig. 3.2. Also shown is a theoretical fit in which the gain $G = \frac{P(L)}{P(0)}$ is numerically computed according to $G = \exp\left[\int_0^L (g(z) - \alpha_l)\, dz\right]$ for an amplifier of length $L = 1$ mm, waveguide loss α_l and spatially dependent gain coefficient

$$g(z) = \frac{g_0}{1 + \left(\frac{P(z)}{P_s}\right)^{\beta}} \tag{3.1}$$

where g_0 and P_s are the modal gain coefficient and the saturation power. In the simplest approximation in which the gain is a linear function of the carrier density, $\beta = 1$ according to Eqns. 2.1 and 2.3. For a compressively-strained quantum well, $g(N) \propto 1 - 2e^{-N/M}$ is found to be a better approximation, where M is a parameter dependent on the number of quantum wells and the density of states [22][23]. This, however, leads to a saturation behavior that can no longer be expressed in the form $g(P(z))$ convenient for numercal calculations. The saturation behavior is characterized by a more rapid saturation and this can be effectively modeled simply by using $\beta > 1$ in Eqn. 3.1.

The parameters for the SOA estimated from Eqn. 3.1 and the measured data are as follows: Fiber-SOA coupling loss of 2 dB for both the input and output facets, saturation enhancement $\beta = 1.2$, waveguide internal loss coefficient of $\alpha_l = 8.2$ cm^{-1}, saturation power of $P_s = 9.3$ dBm and unsaturated gain coefficient of $g_0 = 67.4$ cm^{-1}. These parameters are used in subsequent calculations for modeling the conversion efficiency and the optical signal-to-noise ratio.

3.2.2 Wavelength Converter Optimization

Wavelength Converter Design

The wavelength converter based on four-wave mixing in a semiconductor optical amplifier is shown in Fig. 3.3(a). The pump source is a tunable, external-cavity semiconductor laser with approximately +3 dBm in-fiber power. The cw pump and the input signal are combined in a fiber bi-directional coupler (BDC) after individually going through a mechanical polarization controller (PC). The PCs are used to align the polarizations of both the pump and the signal to the TE axis of the SOA. The combined pump and signal are then amplified together in a high-power Erbium-doped fiber amplifier (EDFA) with saturated output power of $\sim$ 19 dBm, and subsequently filtered in the passband of a 10 nm wide optical bandpass filter (ASE Prefilter). This process of ASE prefiltering suppresses the ASE from the EDFA in the spectral region of the converted signal thus enhancing the optical signal-to-noise ratio of the converted signal. The concept was first proposed and demonstrated by Zhou *et al.* [24] using a fiber bragg grating as the filter element and subsequently by Shieh *et al.* [25] using a wide bandpass filter. The filtered pump and signal are then coupled into the SOA with approximately +13 dBm maximum total power. At the output of the SOA, a 1 nm wide optical bandpass filter (OBF) is used to isolate the converted signal from the pump and the input signals.

An optical spectrum at the output of the SOA is shown in Fig. 3.3(b) for a 20 nm shift down in wavelength. The spectrum illustrates qualitatively the importance of ASE prefiltering; the ASE level at the converted signal is reduced by $>$ 10 dB from

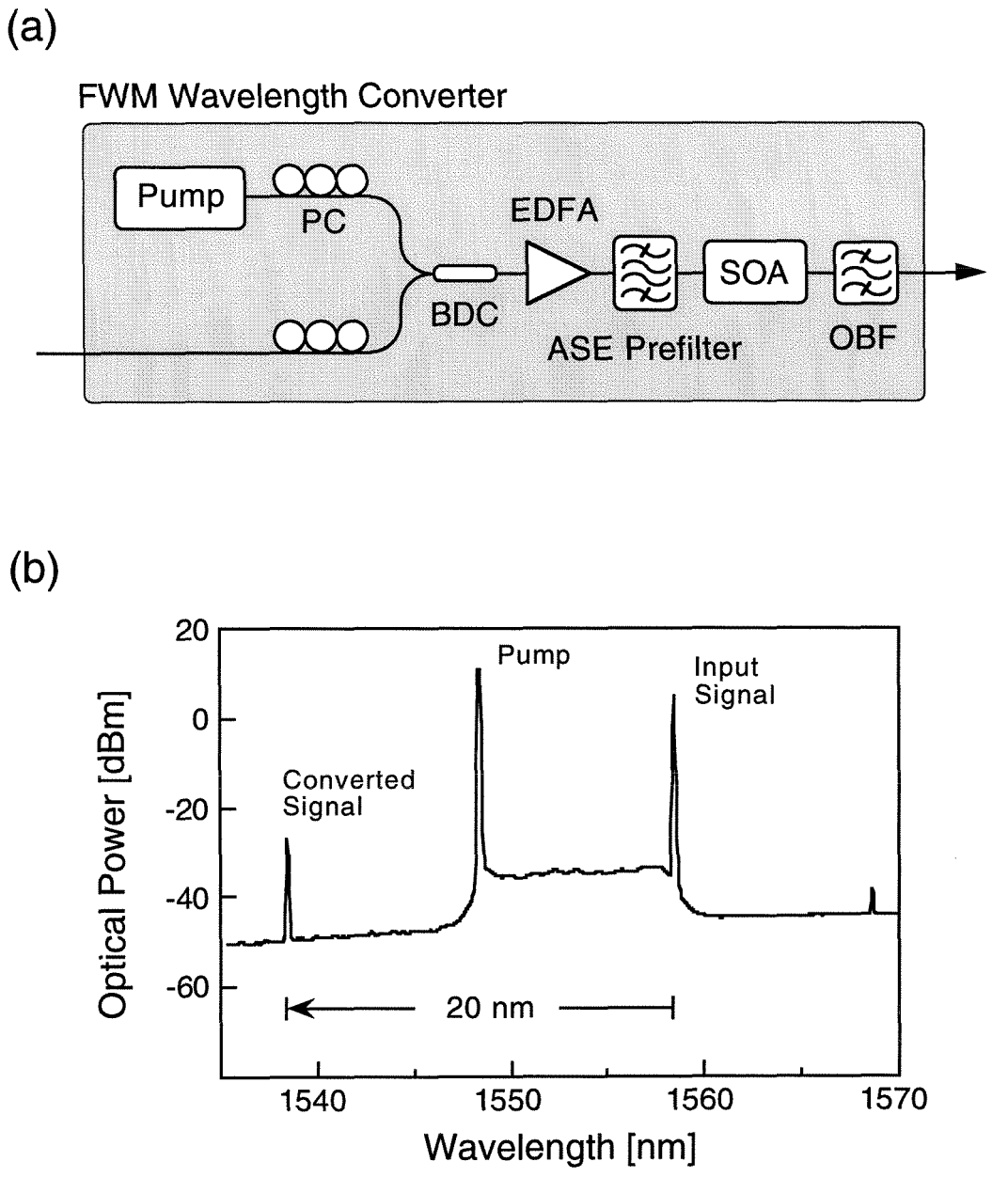

Figure 3.3: (a) The detailed configuration of a wavelength converter based on four-wave mixing in a semiconductor optical amplifier. (b) The optical spectrum at the output of the SOA for a 20 nm downshift measured into 0.1 nm resolution bandwidth.

the ASE level in the passband of the ASE prefilter. The improvement is quantified in the next section.

Input Power and ASE Prefiltering

Although $\chi^{(3)}$ nonlinearities in semiconductor optical amplifiers are 4–5 orders of magnitude greater than in materials such as silica fiber, in a typical SOA with length $\sim$ 1 mm, careful optimizations have to be made in order to achieve sufficient converted signal power and signal-to-noise ratio. At a given point along the SOA the converted signal generated is proportional to optical powers $P_{\text{pump}}^2 P_{\text{signal}}$. However, pump, signal and the converted signal are being amplified along the SOA. In the small signal regime in which the SOA is not saturated, the efficiency can be approximated by using the pump and signal powers at the output of the SOA [26] because the optical powers are at their maximum at this point. However, when the SOA is operated in a heavily saturated regime with less than 5 dB gain, the accurate computation of the conversion efficiency requires solving numerically Eqns. 2.6 and 2.7 to properly account for the nonlinear interaction along the complete length of the SOA.

To study in detail the impact of the input power on the fidelity of the converted signal and to quantify the benefits of ASE prefiltering mentioned in the previous section, a simple measurement is made. A cw signal from a distributed-feedback (DFB) laser at 1558.5 nm is input to the wavelength converter shown in Fig. 3.3(a) with a variable attenuator inserted after the ASE prefilter to vary the optical power input to the SOA. The pump wavelength is set for a 6 nm downshift of the signal and the ratio of the pump-to-signal power is maintained at 6 dB. The optical spectrum

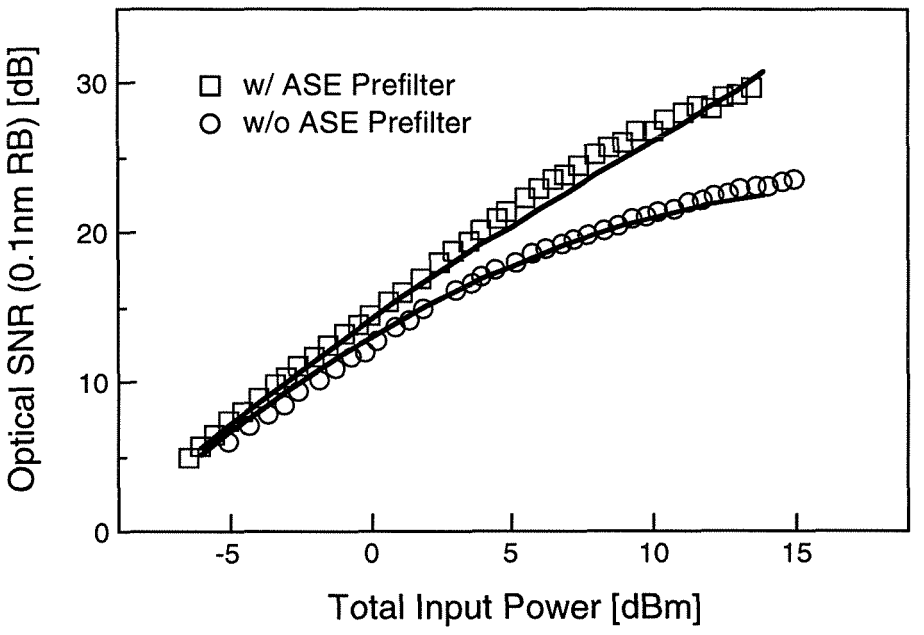

Figure 3.4: Experimental (open symbols) and theoretical (solid line) optical SNR as a function of total input power. The two cases, with and without ASE prefiltering, are shown.

at the output of the SOA is examined as the total input power is varied for the two cases of with and without the ASE prefilter.

As the input power is increased, the converted signal power also increases. In addition, as the SOA becomes saturated, the ASE generated by the SOA is reduced. A quantity which effectively describes the fidelity of the resulting converted signal is the optical signal-to-noise ratio (SNR). In an optically preamplified receiver system which is no longer limited by the thermal-noise of the photodetector, optical SNR sets an absolute limit to the lowest bit-error-rate that can be achieved [27]. The ASE noise level is measured into 0.1 nm resolution bandwidth about the converted signal.

In Fig. 3.4 is shown the experimentally measured optical SNR with and without an ASE prefilter. The ASE spectral density in the region of the converted signal at the output of the SOA is given by

$$S_{\text{out}} = GS_{\text{in}} + n_{\text{sp}}(G-1)h\nu \tag{3.2}$$

where S_{in} is the ASE input, G the gain of the SOA and n_{sp} the spontaneous emission factor. At the small input powers gain is large and thus S_{out} is dominated by the second term regardless of whether ASE prefiltering is used. However, at the large input powers, the ASE generated by the SOA (second term) is reduced thus the amplified input ASE (first term) becomes dominant without the application of an ASE prefilter. At the total input power of 14 dBm, this difference is approximately 7 dB as shown in the figure.

The optical SNR is modeled using Eqns. 2.6 and 2.7, and Eqn. 3.2. The spontaneous-emission factor n_{sp} is a function of the inversion in the SOA or equivalently the saturated gain coefficient. This can be taken into account in a simple form by normalizing n_{sp} according to

$$n_{\text{sp}}(\bar{g}) = n_{\text{sp}}^0 \frac{g_0}{\bar{g}}$$

where $\bar{g}$ is an average gain coefficient along the length of the SOA given by

$$\bar{g} = \frac{1}{L}\int_0^L \frac{g_0}{1+\left(\frac{P(z)}{P_s}\right)^\beta}\, dz. \tag{3.3}$$

The calculated optical SNRs using the parameters determined for the SOA in the previous section and $n_{\text{sp}}^0 = 2.8$, are shown as a solid line in Fig. 3.4.

Semiconductor Optical Amplifier Length

We have examined how the performance of a FWM wavelength converter can be maximized in two ways. First, one would like to operate with the highest input powers available to increase the strength of the nonlinear interaction. Second, ASE noise in the spectral region of the converted signal at the input should be minimized by ASE prefiltering. These optimizations are carried out outside the SOA.

Optimization can also be achieved within the SOA device itself. To achieve high optical powers in the SOA, the saturation power P_s should be maximized and the internal waveguide loss α_l should be minimized. These optimizations, however, are already an integral part of fabricating a high performance semiconductor optical amplifier. For application in the wavelength converter, we examine the benefits of a longer device. In Fig. 3.5(a) is shown the predicted optical SNR for SOA lengths ranging from 0.5 mm to 3.0 mm. The calculation is for an operating point of +14 dBm total in-fiber input power with ASE prefiltering. The optical SNR of 30.6 dB for a 1 mm long device is shown as a reference. In Fig. 3.5(b) are shown the conversion efficiency and the optical SNR referenced to their respective values in a 1 mm device. An improvement of almost 7.5 dB in SNR for a 3 mm device is predicted. The difference between the conversion efficiency and optical SNR improvements results from the additional noise that is generated and amplified in a longer SOA.

The improvement in optical SNR is especially important in the cascading of the wavelength converters as will be discussed in Chapter 5. These predictions have not yet been verified, however, due to lack of longer SOAs having identical active layer structures.

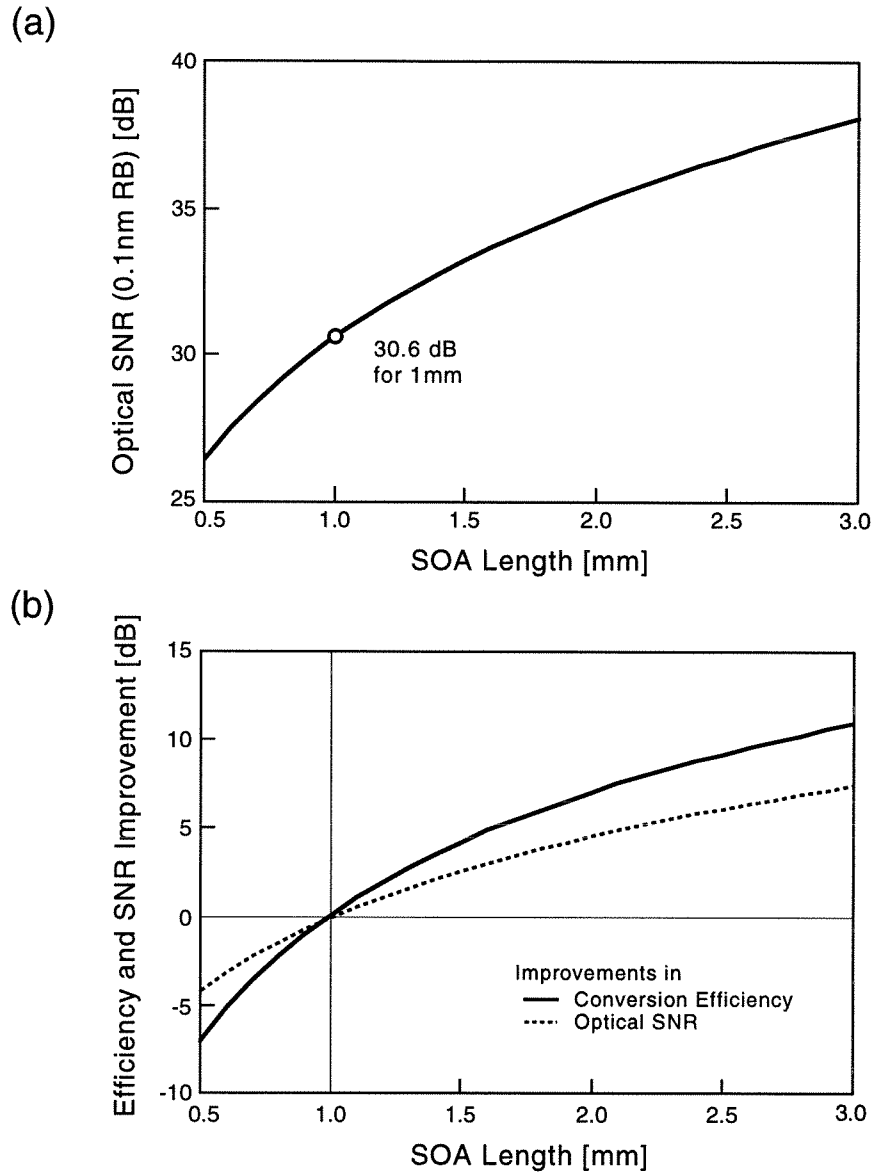

Figure 3.5: (a) The predicted optical SNR for a 6 nm downshift as a function of SOA length. (b) Predicted improvements in fiber-to-fiber conversion efficiency and optical SNR relative to 1 mm SOA device used in the experiments.

Bibliography

[1] S. B. Alexander *et al.*, "A precompetitive consortium on wide-band all-optical networks," *J. Lightwave Technol.*, vol. 11, pp. 714–732, 1993.

[2] P. E. Green, Jr., "Optical Networking Update," *IEEE J. Select. Areas Commun.*, vol. 14, pp. 764–779, 1996.

[3] J. C. Feggeler *et al.*, "WDM transmission measurements on the installed segment-H of the TPC-5 optical amplifier undersea cable system," *Electron. Lett.*, vol. 32, pp. 1314–1315, 1996.

[4] Y. Tachikawa, Y. Inoue, M. Ishii and T. Nozawa, "Arrayed-wave-guide grating multiplexer with loop-back optical paths and its applications," *J. Lightwave Technol.*, vol. 14, pp. 977–984, 1996.

[5] I. Baumann, J. Seifert, W. Nowak and M. Sauer, "Compact all-fiber add-drop-multiplexer using fiber bragg gratings," *IEEE Photon. Technol. Lett.*, vol. 8, pp. 1331–1333, 1996.

[6] T. A. Tumolillo, M. Donckers and W. H. G. Horsthuis, "Solid-state optical space switches for network cross-connect and protection applications," *IEEE Communications Magazine*, vol. 35, pp. 124–130, 1997.

[7] H. Onaka *et al.*, "1.1 Tb/s WDM transmission over a 150 km 1.3 μm zero-dispersion single-mode fiber," *Optical Fiber Communication Conference 1996*, San Jose, California, postdeadline paper PD19.

[8] A. H. Gnauck *et al.*, "One terabit/s transmission experiment," *Optical Fiber Communication Conference 1996*, San Jose, California, postdeadline paper PD20.

[9] T. Morioka *et al.*, "100 Gbit/s × 10 channel OTDM/WDM transmission using a single supercontinuum WDM source," *Optical Fiber Communication Conference 1996*, San Jose, California, postdeadline paper PD21.

[10] G. Wellbrock, "Field deployable OC-192 optically amplified transport network," *Optical Fiber Communication Conference 1997*, Dallas, Texas, paper TuL6.

[11] R. A. Barry and Pierre A. Humblet, "Models of blocking probability in all-optical networks with and without wavelength changers," *IEEE J. Select. Areas Commun.*, vol. 14, pp. 858–867, 1996.

[12] M. Kovačević and A. Acampora, "Benefits of wavelength translation in all-optical clear-channel networks," *IEEE J. Select. Areas Commun.*, vol. 14, pp. 868–880, 1996.

[13] S. J. B. Yoo, "Wavelength conversion technologies for WDM network applications," *J. Lightwave Technol.*, vol. 14, pp. 955–966, 1996.

[14] J. M. Wiesenfeld, J. S. Perino, A. H. Gnauck and B. Glance, "Bit error rate performance for wavelength conversion at 20 Gbit/s," *Electron. Lett.*, vol. 30, pp. 720–721, 1994.

[15] D. Norte and A. E Willner, "Demonstration of an all-optical data format transparent WDM-to-TDM network node with extinction ratio enhancement for reconfigurable WDM networks," *IEEE Photon. Technol. Lett.*, vol. 8, pp. 715–717, 1996.

[16] T. Durhuus, B. Mikkelsen, C. Joergensen, S. L. Danielsen and K. E. Stubkjaer, "All-optical wavelength conversion by semiconductor optical amplifiers," *J. Lightwave Technol.*, vol. 14, pp. 942–954, 1996.

[17] C. Q. Xu, H. Okayama, K. Shinozaki, K. Watanabe and M. Kawahara, "Wavelength conversions ~1.5 μm by difference frequency generation in periodically domain-inverted $LiNbO_3$ channel waveguides," *Appl. Phys. Lett.*, vol. 63, pp. 1170–1172, 1993.

[18] S. J. B. Yoo, "Wavelength conversion by difference-frequency-generation in AlGaAs wave-guides with periodic domain inversion achieved by wafer bonding," *Appl. Phys. Lett.*, vol. 68, pp. 2609–2611, 1996.

[19] M. C. Tatham, G. Sherlock and L. D. Westbrook, "20 nm wavelength conversion using nondegenerate four-wave mixing," *IEEE Photon. Technol. Lett.*, vol. 5, pp. 1303–1306, 1993.

[20] M. A. Summerfield and R. S. Tucker, "Optimization of pump and signal powers for wavelength converters based on FWM in semiconductor optical amplifiers," *IEEE Photon. Technol. Lett.*, vol. 8, pp. 1316–1318, 1996.

[21] K. Inoue, "Wavelength conversion experiment using fiber four-wave mixing," *IEEE Photon. Technol. Lett.*, vol. 4, pp. 69–72, 1992.

[22] K. J. Vahala and C. E. Zah, "Effect of doping on the optical gain and the spontaneous noise enhancement factor in quantum well amplifiers and lasers studied by simple analytical expressions," *Appl. Phys. Lett.*, vol. 52, pp. 1945–1947, 1988.

[23] K. J. Vahala and C. E. Zah, "Approximate expressions for modulation speed and threshold for performance optimization of biaxially compressive strain quantum-well lasers," *Appl. Phys. Lett.*, vol. 59, pp. 3230–3232, 1991.

[24] J. Zhou and K. J. Vahala, "Noise reduction in FWM wavelength converters," *Conference on Lasers and Electro-Optics 1995*, Baltimore, Maryland, paper CThT1.

[25] W. Shieh and A. E. Willner, "SNR improvement of four-wave mixing wavelength shifting by noise prefiltering in a semiconductor optical amplifier," *Conference on Lasers and Electro-Optics 1996*, Anaheim, California, paper CThB5.

[26] J. Zhou, N. Park, J. W. Dawson, K. J. Vahala, M. A. Newkirk and B. I. Miller, "Terahertz four-wave mixing spectroscopy for study of ultrafast dynamics in a semiconductor optical amplifier," *Appl. Phys. Lett.*, vol. 63, pp. 1179–1181, 1993.

[27] A. Yariv, *Optical Electronics, 4th ed.*, Holt, Rinehart and Winston, Philadelphia, 1991.

Chapter 4

Wavelength Conversions up to 18 nm at 10 Gb/s

4.1 Introduction

In a high bit-rate digital communication system, the system performance is quantified by the bit-error-rate (BER). In the previous chapter, the optimization of wavelength conversion by four-wave mixing (FWM) in a semiconductor optical amplifier (SOA) was presented with respect to the related quantity, the optical signal-to-noise ratio (SNR). In the system experiments described in Chapters 4–7, the final measure of the converter performance is quantified using the bit-error-rate. Although a BER performance of $< 10^{-15}$ may be desired for data communication applications, in general BER $= 10^{-9}$ is accepted as the threshold for "error-free" transmission.

BER performance for several different techniques of wavelength conversion has been studied with respect to conversion range and wavelength operating points. Wave-

length conversion in a tunable semiconductor laser by cross-gain modulation has been demonstrated at 10 Gb/s over 30 nm [1], in a passive quasi-phase-matched AlGaAs waveguides by difference frequency generation at 2.5 Gb/s over 6 nm [2], in an SOA by cross-gain modulation at 20 Gb/s for up and downshifts of 10 nm [3] and by cross-phase modulation in an SOA interferometric converter at 5 Gb/s for up and downshifts of 13 nm [4]. By four-wave mixing in an SOA, Tatham *et al.* [5], have demonstrated 20 nm downshift at 622 Mb/s and Ludwig *et al.* [6], 4 nm conversion at 10 Gb/s. However, no comprehensive study has been made of the maximum wavelength shift possible at these high bit-rates. Furthermore, to our knowledge, this study is the first to conduct BER studies on wavelength upshifts by FWM in an SOA.

In this chapter the conversion bandwidth of a four-wave mixing semiconductor optical amplifier wavelength converter is characterized. Conversion of 10 Gb/s signals with bit-error-rate performance of $< 10^{-9}$ is demonstrated for record wavelength downshifts of up to 18 nm and upshifts of up to 10 nm [7].

4.2 Experiment

A schematic of the experimental setup to characterize the converter performance is shown in Fig. 4.1(a). A 10 Gb/s Hewlett-Packard bit-error-rate tester (BERT) consisting of a clock source, pattern generator, BER analyzer and a microwave transition analyzer is used for signal generation, error detection and eye diagram analysis. A non-return-to-zero (NRZ) pseudo-random bit stream (PRBS) from the BERT is amplified and used to drive a $LiNbO_3$ Mach-Zehnder external modulator (MOD) at

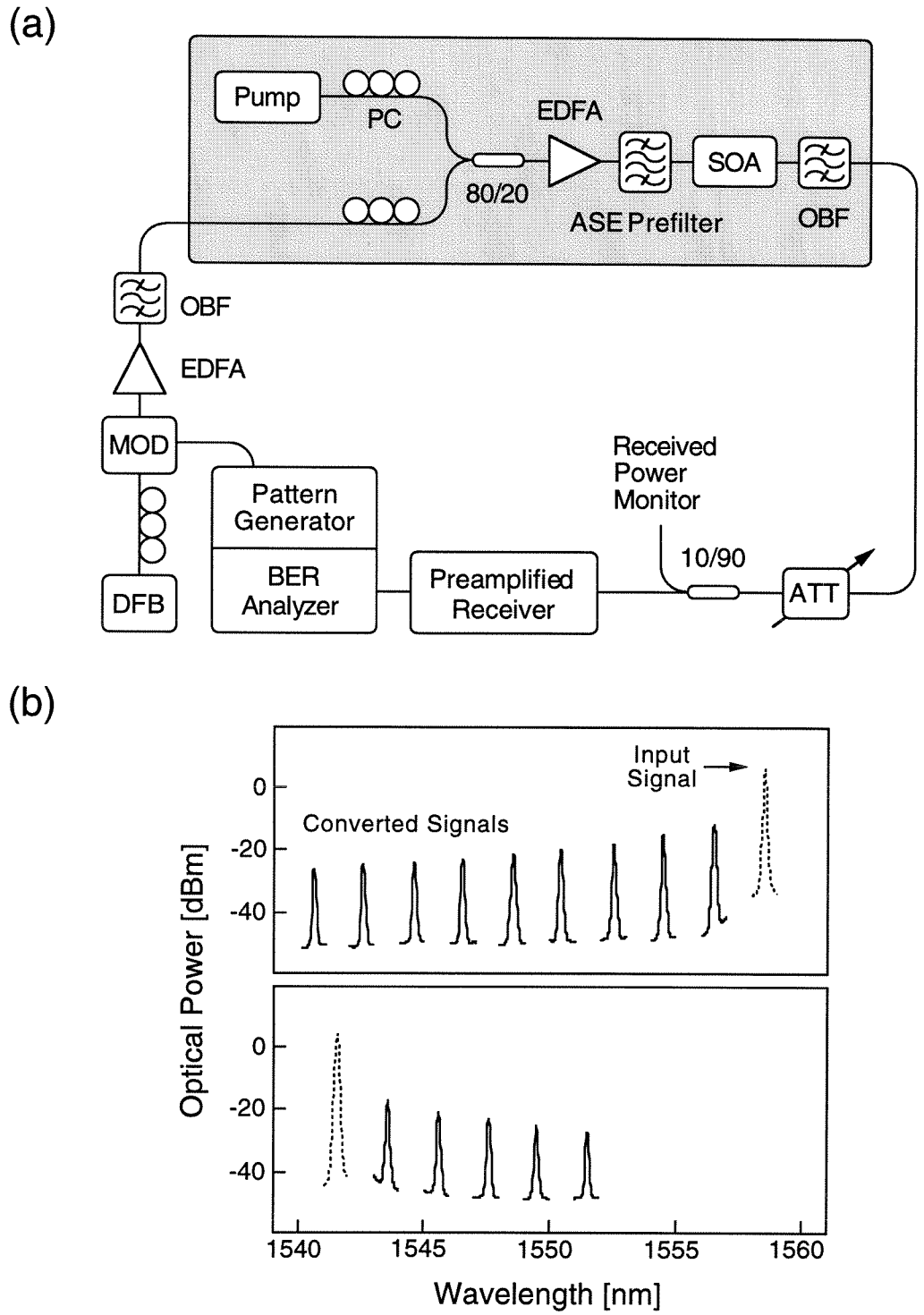

Figure 4.1: (a) A schematic of the experimental setup for wavelength conversion at 10 Gb/s. (b) The optical spectra of the input signal and the wavelength converted signals for wavelength down and upshifts at 2 nm intervals measured into 0.1 nm resolution bandwidth.

10 Gb/s. The optical signal source, a distributed feedback (DFB) laser, is input to the modulator at the proper polarization by using a mechanical polarization controller (PC). The modulated signal is then amplified and filtered with an Erbium-doped fiber amplifier (EDFA) optical bandpass filter (OBF) pair to compensate for the insertion loss of the modulator. The signal is then input to the wavelength converter indicated by the shaded box. The detailed configuration of the converter has already been described in Chapter 3. A 80/20 bi-directional coupler is used for the pump and the signal, and the converter is operated with approximately +13 dBm total power (maximum available) into the SOA biased at 300 mA. The pump-to-signal power ratio measured at the output of the SOA is maintained at 6–8 dB. The converted signal at the output of the wavelength converter then goes through a variable attenuator (ATT) and a 10/90 tap. The received power of the converted signal into the preamplified receiver is measured at the tap into a 0.5 nm bandwidth using an optical spectrum analyzer. Finally, the converted signal is detected with a preamplified receiver consisting of a two-stage low-noise EDFA optical preamplifier, a 1 nm OBF, a 11 GHz *p-i-n* receiver and a 6 GHz electrical amplifier. The amplified electrical signal is then used for error detection and eye diagram analysis.

The converter performance is characterized for wavelength shifts both down and up at 2 nm intervals. In Fig. 4.1(b) are summarized the spectra of the input signal (dotted line) and the converted signals (solid line) at the output of the SOA for wavelength downshifts of 2 to 18 nm and for upshifts of 2 to 10 nm. The converted signals shown are the range over which BER performance of $< 10^{-9}$ is achieved. For

the downshifts, the DFB signal source has a wavelength of 1558.5 nm. The ASE in the region of the converted signals is approximately constant except for the 2 nm shift resulting from the shape of the ASE prefilter. The decrease in conversion efficiency for increasing wavelength shifts can be seen in the decreasing optical SNRs ranging from 32 to 24.5 dB into 0.1 nm bandwidth. For the upshifts, the signal source has a wavelength of 1541.5 nm and the optical SNRs of the converted signals range from 27.1 to 20.5 dB. For a wavelength shift of equal magnitude, the conversion efficiency is over 3 dB lower for the upshift case. This asymmetry in the conversion efficiency which results from the interference among the different mechanisms participating in the FWM process [8] limits the overall wavelength range of the converter operation to that set by the maximum wavelength upshift.

Qualitatively, the converter performance can be seen by examining the eye diagrams. Fig. 4.2 shows eye diagrams for the unconverted signal at 1558.5 nm and the converted signal downshifted by 18 nm. The converted eye is clearly open and there is almost no visible additional noise. The lower part of the figure shows the unconverted signal at 1541.5 nm and the converted signal upshifted by 10 nm. There is a small amount of additional noise evident at the '1' level, however, the eye still remains clearly open.

Quantitatively, the system performance of the wavelength converter is studied by examining the BER versus received power curves and determining the receiver sensitivity, *i.e.*, the received power necessary to achieve BER = 10^{-9}. In Fig. 4.3 are shown representative BER curves for wavelength downshifts of 2, 10 and 18 nm and

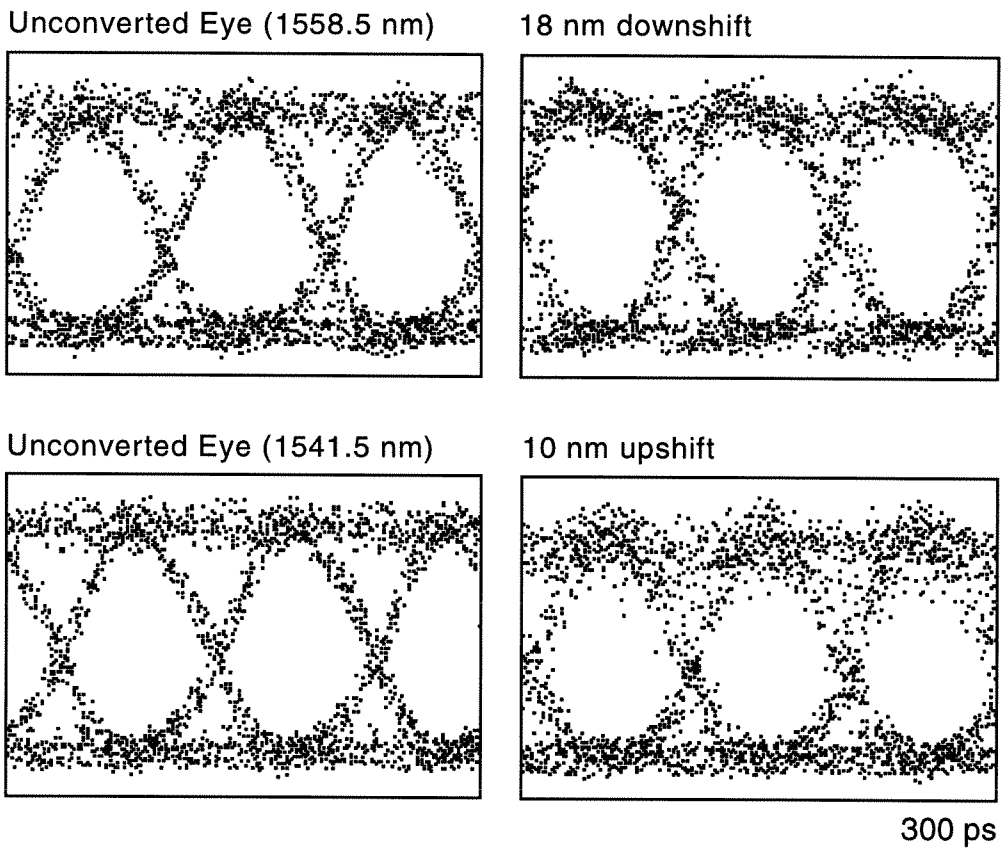

Figure 4.2: Eye diagrams at 10 Gb/s of the unconverted and converted signals for a 18 nm downshift (top) and a 10 nm upshift (bottom).

for upshifts of 2, 6 and 10 nm. The experimental data shown is for a PRBS $2^7 - 1$ pattern. Longer patterns have been examined, however, power penalties are smaller than 0.3 dB for PRBS patterns of length up to $2^{31} - 1$. For the 2 nm shifts, the suppression of the pump wave at the converter output by the OBF is insufficient to prevent significant degradation of the receiver sensitivity. With a single filter, there is a received power penalty of approximately 3 dB compared to the other wavelength

shifts. By addition of an extra OBF at the SOA output in the wavelength converter for the case of 2 nm shift, the receiver sensitivity is improved by about 2 dB, bringing it to within 1 dB of the other curves. In the cases of maximum up and downshifts, there is a slight flooring of the BER curves due to the decreased optical SNR of the converted signal. The floor occurring at BER = 7×10^{-10} is more evident for the 10 nm upshift due to the smaller optical SNR. Also, there are slight differences in the slopes of the BER curves for the different wavelength shifts which result from the spectral dependence of the optical preamplifier in the preamplified receiver (Appendix A). Due to this spectral dependence, to accurately assess the penalty in the conversion process, a proper baseline, *i.e.*, the BER curve of an unconverted signal at the converted wavelength is required. Due to the fixed wavelength of the DFB laser used as the input signal source, a proper baseline can not be measured.

In conclusion, the wavelength converter characterized in this work has demonstrated conversion of 10 Gb/s signals over a record span of 18 nm. The enhanced performance is believed to result from the use of high SOA input power in conjunction with ASE prefiltering. The demonstration of both upshift and downshift capability, effectively shows how the converter may be used to shift among any WDM channels spanning a 10 nm spectral range.

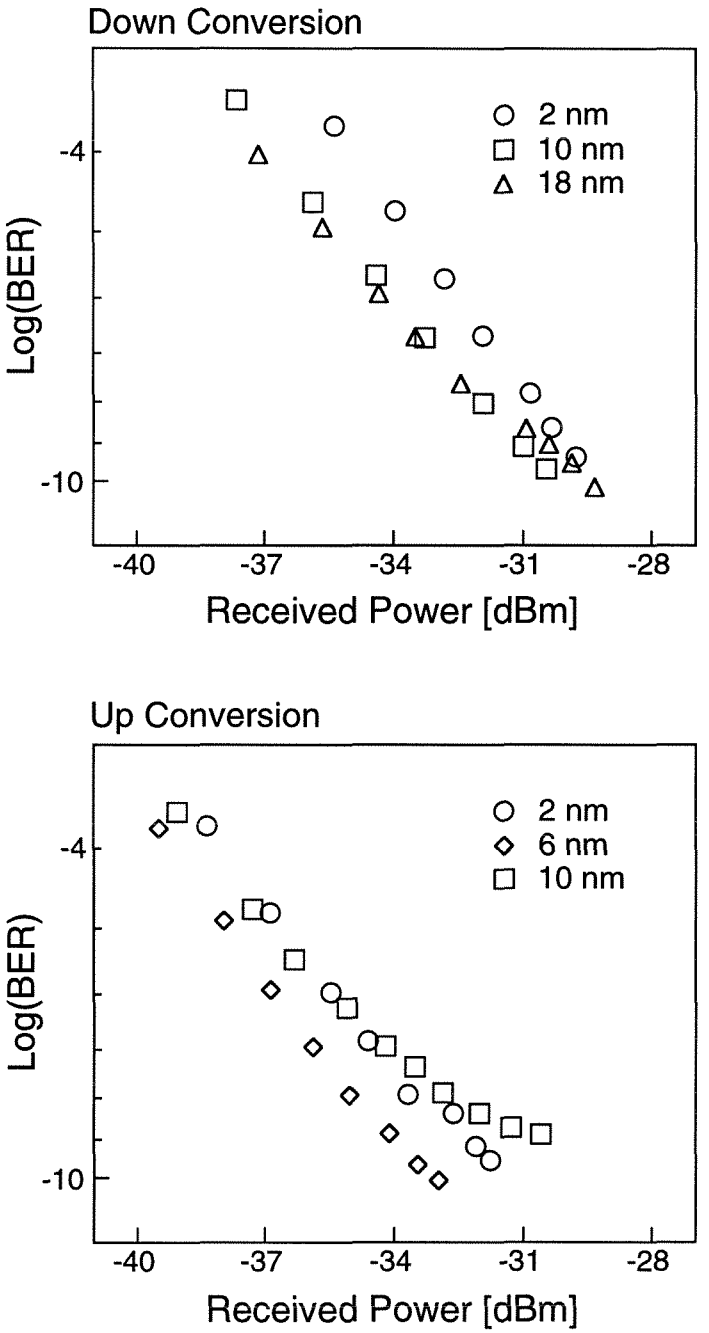

Figure 4.3: Bit-error-rate vs. received power for wavelength downshifts of 2, 10 and 18 nm, and for wavelength upshifts of 2, 6 and 10 nm at 10 Gb/s.

Bibliography

[1] H. Yasaka, H. Sanjoh, H. Ishii, Y. Yoshikuni and K. Oe, "Finely tunable wavelength conversion of high bit-rate signals by using a superstructure-grating distributed-bragg-reflector laser," *J. Lightwave Technol.*, vol. 15, pp. 334–341, 1997.

[2] S. J. B. Yoo, A. Rajhel, C. Caneau, R. Bhat and M. A. Koza, "Multichannel polarization-independent wavelength conversion by difference-frequency generation in AlGaAs waveguides," *Optical Communication Conference 1997*, Dallas, Texas, paper TuO6.

[3] J. M. Wiesenfeld, J. S. Perino, A. H. Gnauck and B. Glance, "Bit error rate performance for wavelength conversion at 20 Gbit/s," *Electron. Lett.*, vol. 30, pp. 720–721, 1994.

[4] T. Durhuus, B. Mikkelsen, C. Joergensen, S. L. Danielsen and K. E. Stubkjaer, "All-optical wavelength conversion by semiconductor optical amplifiers," *J. Lightwave Technol.*, vol. 14, pp. 942–954, 1996.

[5] M. C. Tatham, G. Sherlock and L. D. Westbrook, "20 nm wavelength conversion using nondegenerate four-wave mixing," *IEEE Photon. Technol. Lett.*, vol. 5, pp. 1303–1306, 1993.

[6] R. Ludwig and G. Raybon, "BER measurements of frequency converted signals using four-wave mixing in a semiconductor laser amplifier at 1, 2.5, 5, and 10 Gbit/s," *Electron. Lett.*, vol. 30, pp. 338–339, 1994.

[7] David F. Geraghty, Robert B. Lee, Kerry J. Vahala, Marc Verdiell, Mehrdad Ziari and Atul Mathur, "Wavelength conversions up to 18 nm at 10 Gb/s by

four-wave mixing in a semiconductor optical amplifier," *IEEE Photon. Technol. Lett.*, vol. 9, pp. 452-454, 1997.

[8] J. Zhou, N. Park, J. W. Dawson, K. J. Vahala, M. A. Newkirk and B. I. Miller, "Terahertz four-wave mixing spectroscopy for study of ultrafast dynamics in a semiconductor optical amplifier," *Appl. Phys. Lett.*, vol. 63, pp. 1179–1181, 1993.

Chapter 5

Cascaded Wavelength Conversions at 10 Gb/s

5.1 Introduction

For a single wavelength conversion using four-wave mixing in a semiconductor optical amplifier, minimal degradation in system performance has been demonstrated previously at bit-rates of up to 10 Gb/s [1][2]. However, a signal path in an all-optical network will contain multiple crossconnects making cascadability of any wavelength conversion technique indispensable to practical implementation in a WDM network. Cascadability has already been demonstrated by cross-gain modulation in an SOA at 2 Gb/s by Wiesenfeld *et al.* [3] and in a wavelength-tunable semiconductor laser at 10 Gb/s by Yasaka *et al.* [4]. Recently, Pedersen *et al.*, has demonstrated 10 cascaded conversions in a recirculating loop using an interferometric wavelength converter based on SOAs at 10 Gb/s [5].

In this chapter, the first demonstration of cascaded wavelength conversion in a semiconductor optical amplifier by four-wave mixing is presented. Bit-error-rate performance of $< 10^{-9}$ at 10 Gb/s is achieved for two conversions of up to 10 nm down and up in wavelength. For two wavelength conversions of 5 nm down and up, a power penalty of 1.3 dB is measured. A system of two wavelength converters spanning 40 km of single-mode fiber is also demonstrated [6]–[8].

5.2 Experiment

The schematic of the experimental setup is shown in Fig. 5.1(a). The detailed configuration of the FWM wavelength converter, simply labeled wavelength converter 1 and 2 in the shaded boxes, are identical to the configuration used in Chapter 4. The ASE prefilter used in converters 1 and 2 have 10 and 16 nm FWHM, respectively. The semiconductor optical amplifier in converter 2 is an identical 1 mm long compressively-strained multiple quantum well SOA biased at 300 mA.

The source for the input signal is provided by a DFB laser at 1558.7 nm and modulated externally at 10 Gb/s using a $LiNbO_3$ Mach-Zehnder modulator. In wavelength converter 1 the signal is downshifted in wavelength, and in wavelength converter 2 the signal is upshifted by an equal amount ranging from 4 to 10 nm. At the output of converter 1, the converted signal is amplified and filtered using an EDFA-OBF combination. In the experiment, a single laser source is divided in power to provide the pump waves for the two converters. In order to reduce the interference between the pump wave for converter 2 and the residual pump wave from converter 1 due to

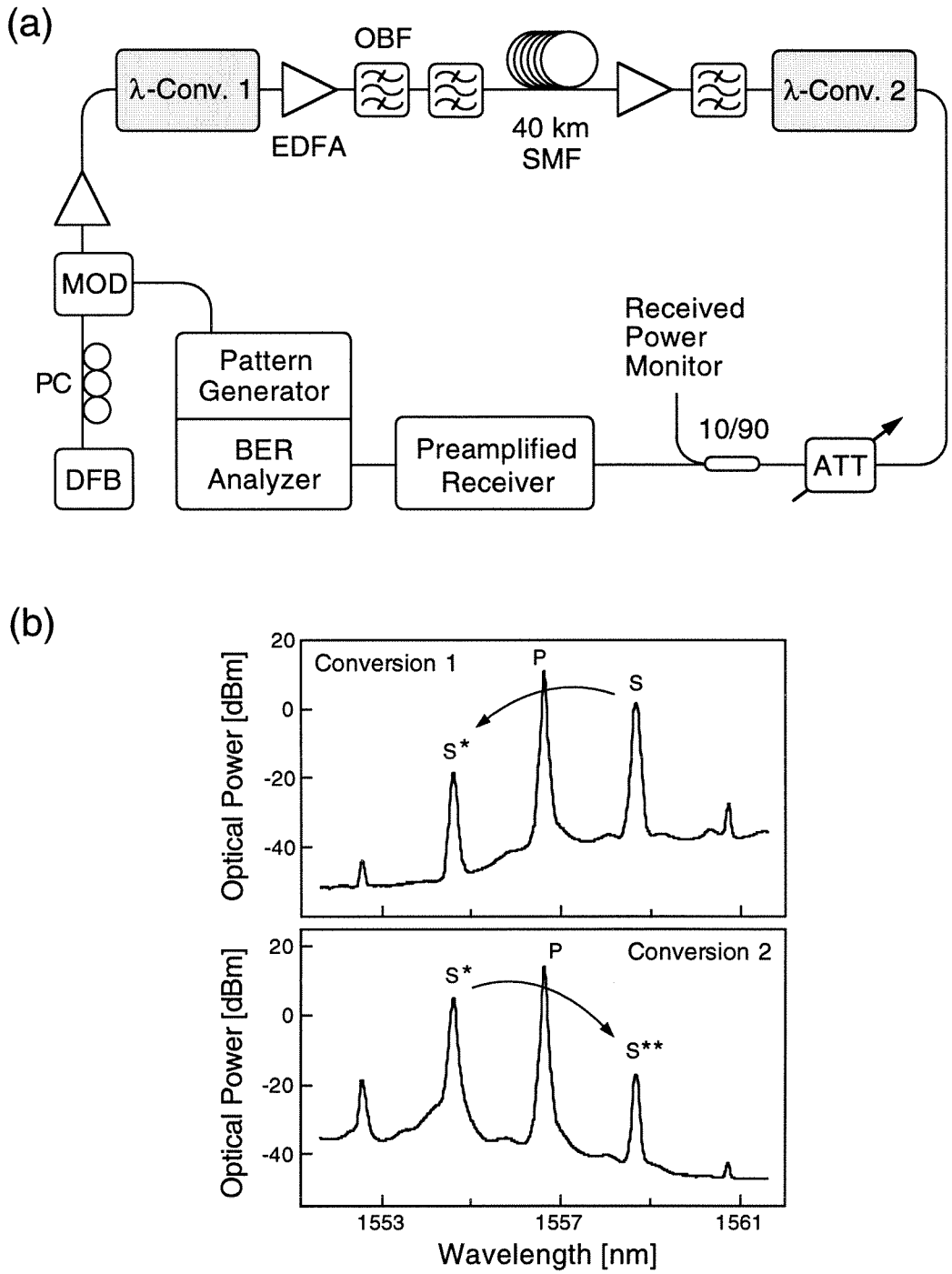

Figure 5.1: (a) The experimental setup for cascaded wavelength conversion spanning 40 km transmission. (b) Optical spectra measured at the output of the semiconductor optical amplifier in the indicated wavelength converter for a wavelength shift of 4 nm.

incomplete suppression achieved by filtering, an extra OBF is used. The 40 km transmission link spanning the two converters consists of 40 km of dispersive single-mode fiber (SMF) and an EDFA-OBF pair to compensate for the propagation losses. The converted signals are detected using a preamplified receiver, and the signal generation and error detection are done using a Hewlett-Packard 10 Gb/s bit-error-rate tester as previously described. In Fig. 5.1(b) are shown the optical spectra measured into 0.1 nm resolution bandwidth at the output of the SOAs in wavelength converter 1 and 2 for a 4 nm wavelength shift down and up, respectively. The pump is labeled P, the original signal S, the converted signal S* and the twice-converted signal S**.

The system performance of the converters are evaluated using a 10 Gb/s pseudo-random non-return-to-zero (NRZ) pattern of length $2^{31}-1$. To assess the degradation in system performance resulting from the wavelength conversion, BER vs. received power curves are measured after wavelength conversion 1 and wavelength conversion 2 with and without the 40 km transmission. In Fig. 5.2 are shown the BER data for the above cases corresponding to a 4 nm shift. Also shown is a baseline curve of the unconverted signal. We note that the converted signal after conversion 1 has a better BER performance. This results from the spectral dependence of the EDFA used in the preamplified receiver, and the DC operating point of the external modulator which is adjusted for maximum performance of the second conversion. The fixed wavelength of the DFB source does not allow for the measurement of a proper baseline for wavelength conversion 1. However, for the twice-converted signals, because they correspond exactly to the unconverted signal in wavelength, the BER data can be

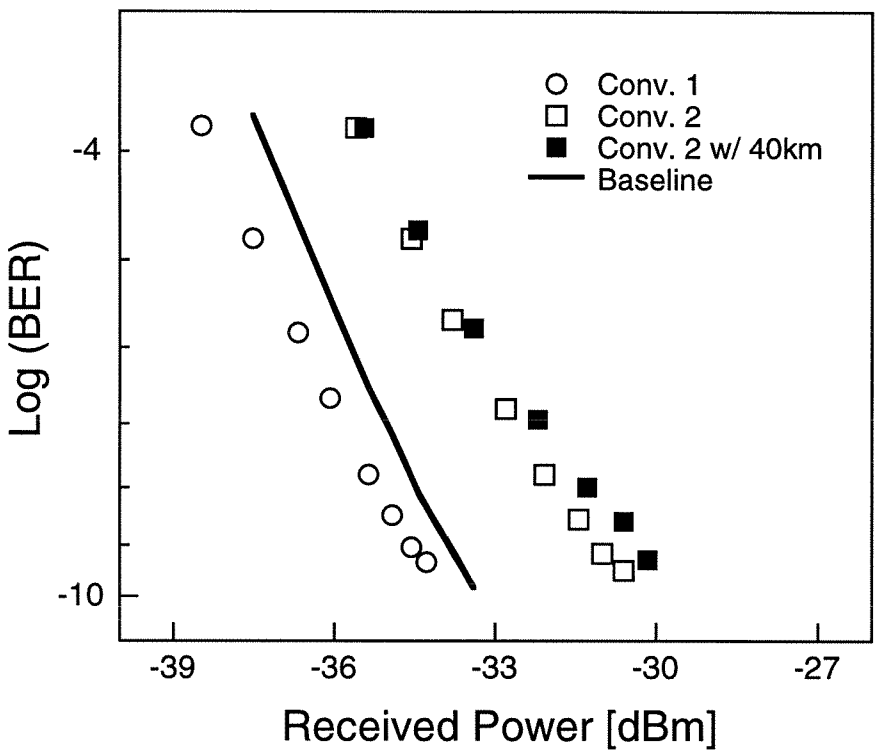

Figure 5.2: Bit-error-rate vs. received power following wavelength conversion 1 and wavelength conversion 2 with and without 40 km transmission in single-mode fiber for a wavelength shift of 4 nm. A baseline curve for the input signal is also shown.

directly compared to the baseline shown.

The above experiment is conducted for wavelength shifts ranging from 4 to 10 nm at 1 nm intervals by varying the pump wavelength. To quantify the overall system performance, we measure the receiver sensitivity, *i.e.*, the received power necessary to achieve BER = 10^{-9}. In Fig. 5.3 are summarized the results of the experiment. Due to the increasing difficulty associated with suppressing the pump wave from conversion 1 for shorter wavelength shifts, the minimum in the sensitivity for conversion 2 does not occur at the shortest wavelength shift where conversion efficiency and optical SNR are maximum. For the longer wavelength shifts, the sensitivity degrades due to the decreasing optical SNR. For the case of conversion 2 with 40 km transmission, the additional decrease in the optical SNR resulting from the extra amplification stage further degrades the sensitivity, and for a 10 nm shift, an error-rate of 10^{-9} could not be achieved. The power penalties for the optimum performance at a wavelength shift of 5 nm are 2.2 and 1.3 dB for conversion 2 with and without 40 km transmission, respectively.

At a 10 nm wavelength shift, cascadability is limited to two conversions, one down and one up in wavelength. This is consistent with the limits due to the lower conversion efficiency for wavelength upshifts characterized in Chapter 4. Although the experiment was limited to two conversions, a simple model which accounts for the optical SNR degradation in the wavelength converter and subsequent amplification without considering possible signal distortion resulting from the conversion process, predicts significantly higher cascadability limits for repeated downshifts or for shorter

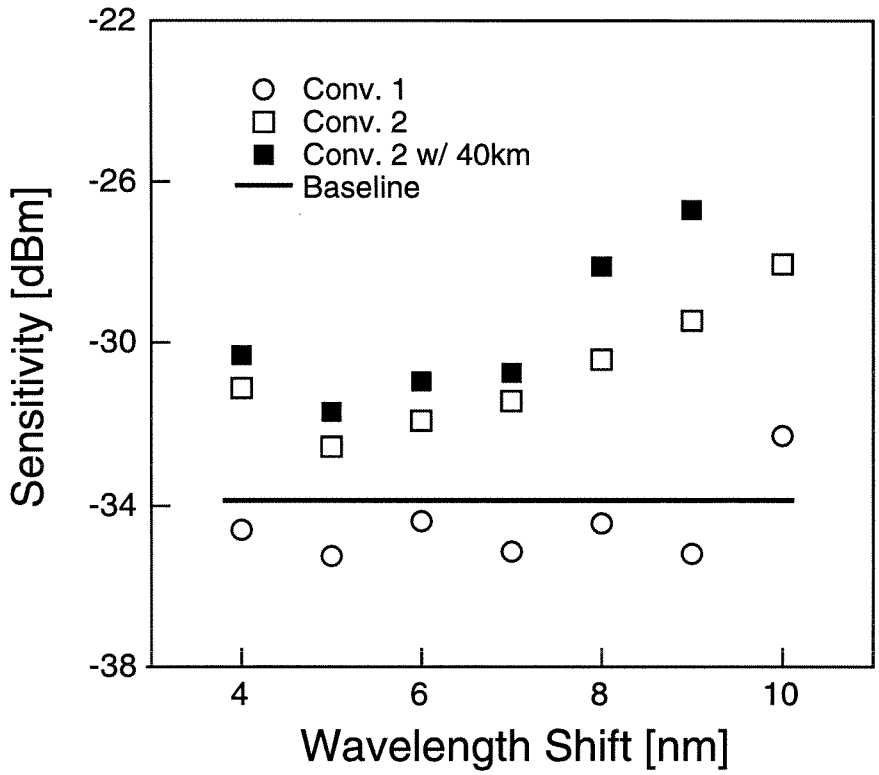

Figure 5.3: Receiver sensitivity (BER = 10^{-9}) vs. wavelength shift for a single wavelength conversion and cascaded wavelength conversion with and without 40 km transmission. Baseline indicates the sensitivity for the original input signal.

wavelength shifts [8]. More importantly, according to the simple model, the number of possible cascaded conversions is almost directly proportional to the conversion efficiency. Therefore, possible improvements in the conversion efficiency resulting from a longer SOA may be essential in the future for making FWM wavelength converters a field deployable technology.

In conclusion, we have demonstrated the cascadability of wavelength conversion by four-wave mixing in a semiconductor optical amplifier. For an externally modulated signal at 10 Gb/s, a bit-error-rate performance of $< 10^{-9}$ and small power penalties were achieved for wavelength shifts ranging from 4 to 10 nm. A transmission experiment was conducted using 40 km of single-mode fiber and small additional degradation in the BER performance was found. The results indicate the feasibility of wavelength conversion by FWM in an SOA for application in an all-optical wavelength-switched network.

Bibliography

[1] R. Ludwig and G. Raybon, "BER measurements of frequency converted signals using four-wave mixing in a semiconductor laser amplifier at 1, 2.5, 5, and 10 Gbit/s," *Electron. Lett.*, vol. 30, pp. 338–339, 1994.

[2] David F. Geraghty, Robert B. Lee, Kerry J. Vahala, Marc Verdiell, Mehrdad Ziari and Atul Mathur, "Wavelength conversions up to 18 nm at 10 Gb/s by four-wave mixing in a semiconductor optical amplifier," *IEEE Photon. Technol. Lett.*, vol. 9, pp. 452-454, 1997.

[3] J. M. Wiesenfeld and B. Glance, "Cascadability and fanout of semiconductor optical amplifier wavelength shifter," *IEEE Photon. Technol. Lett.*, vol. 4, pp. 1168–1171, 1992.

[4] H. Yasaka, H. Ishii, Y. Yoshikuni and K. Oe, "Repeated wavelength conversion of 10 Gbit/s signal using wavelength-tunable semiconductor lasers," *IEEE Photon. Technol. Lett.*, vol. 7, pp. 161–163, 1995.

[5] R. J. S. Pedersen, M. Nissov, B. Mikkelsen, H. N. Poulsen, K. E. Stubkjaer, M. Gustavsson, W. van Berlo and M. Janson, "Transmission through a cascade of 10 all-optical interferometric wavelength converter spans at 10 Gbit/s," *Electron. Lett.*, vol. 32, pp. 1034–1035, 1996.

[6] David F. Geraghty, Robert B. Lee and Kerry J. Vahala, "Cascaded wavelength conversions using four-wave mixing in semiconductor optical amplifiers," *Optical Fiber Communication Conference 1997*, Dallas, Texas, paper WH6.

[7] Robert B. Lee, David F. Geraghty, Kerry J. Vahala, Marc Verdiell, Mehrdad Ziari and Atul Mathur, "Cascaded wavelength conversion by four-wave mixing

in a strained semiconductor optical amplifier at 10 Gb/s," *IEEE Photon. Technol. Lett.*, vol. 9, June, 1997.

[8] David F. Geraghty, Robert B. Lee and Kerry J. Vahala, "Cascaded wavelength conversions by four-wave mixing in semiconductor optical amplifiers at 10 Gb/s," *OSA Trends in Optics and Photonics Series, Systems Technologies*, vol. 12, 1997.

Chapter 6

Crosstalk Penalty in Simultaneous 2-Channel Wavelength Conversion

6.1 Introduction

In a wavelength division multiplexed (WDM) system, it may be desirable to wavelength convert multiple channels at different wavelengths simultaneously in a single converter significantly reducing the number of components and cost. Simultaneous multichannel conversion may also find application in optical signal processing in which the information is encoded using several wavelengths in parallel.

In this chapter we study the application of four-wave mixing (FWM) in a semiconductor optical amplifier (SOA) for simultaneous 2-channel wavelength conversion. Multichannel conversion by FWM has been demonstrated previously. Schnabel *et al.* [1], has demonstrated conversion of 10 channels having a 9 GHz spacing and 140 Mb/s FSK modulation by approximately 2 nm, and Lacey *et al.* [2], 4 channels

having a 2 nm spacing and 2.5 Gb/s ASK modulation. By FWM in dispersion shifted fiber, Inoue *et al.* [3], has demonstrated conversion of 3 channels of 70 GHz spacing and 622 Mb/s FSK modulation by approximately 8 nm. Recently, Yoo *et al.* [4], has demonstrated conversion of 8 channels of 2 nm spacing by difference frequency generation (DFG) in a quasi-phase-matched passive AlGaAs waveguide.

An important issue in all multichannel wavelength conversion techniques is possible crosstalk among the WDM channels. This issue presents a greater problem in semiconductor optical amplifiers than in optical fibers or passive AlGaAs waveguides because of parasitic cross-gain saturation. In wavelength conversion of ASK modulation format signals by FWM, an inverted modulation is imposed on the cw pump by the modulation in the signal power. This parasitic cross-gain modulation imposed by one channel provides an effective crosstalk mechanism in which a second channel experiences a modulation in its conversion efficiency. The problems associated with the above effect have been alluded to previously [2]. Here, a systematic study of its impact on the system performance of the wavelength converter is studied by conducting bit-error-rate (BER) experiments for a range of pump-to-signal power ratios.

The penalty associated with signal crosstalk in 2-channel wavelength conversion by FWM in an SOA is quantified. A strained layer semiconductor optical amplifier is used to wavelength convert two 2.5 Gb/s ASK channels (1.5 nm channel spacing) by 6 and 9 nm. For an SOA operated in deep saturation, a penalty of > 6 dB compared to the case of single-channel conversion is measured for a pump-to-signal power ratio of 8 dB [5].

6.2 Experiment

The schematic of the simultaneous 2-channel wavelength conversion experiment is shown in Fig. 6.1(a). The detailed configuration of the FWM wavelength converter shown in the shaded box is identical to the configuration used in Chapter 4 with one minor change; the polarization controllers (PCs) for the two input signals immediately follow the DFB lasers to independently control the polarization of the 2 channels. The two signal channels are provided by high-speed DFB lasers directly-modulated at 2.5 Gb/s. The two channels are combined in a 50/50 bi-directional coupler and then passed through a variable attenuator. The total power of the combined pump and input signals coupled into the SOA biased at 300 mA is approximately +13 dBm. The polarization state of the pump and both signals is set to the TE polarization of the compressively-strained SOA.

Fig. 6.1(b) shows a typical optical spectrum observed at the output of the SOA measured with a 0.1 nm resolution bandwidth. The spectrum shows the two input channels labeled 1 and 2, their respective converted signals 1* and 2*, and the pump P. The pump is set to 1536.6 nm and the channels 1 and 2 are at wavelengths 1541.1 and 1539.6 nm, respectively. The input signals are shifted by 9 and 6 nm in wavelength. Also visible in the spectrum are additional parasitic FWM products.

Bit-error-rate measurements are performed on both channels using PRBS of length 2^7-1 and $2^{31}-1$. The two channels are modulated by PRBS data and its complement provided by the bit-error-rate tester. The two signals experience different delays due to the different lengths of the SMA cables and optical fiber, which help to simulate

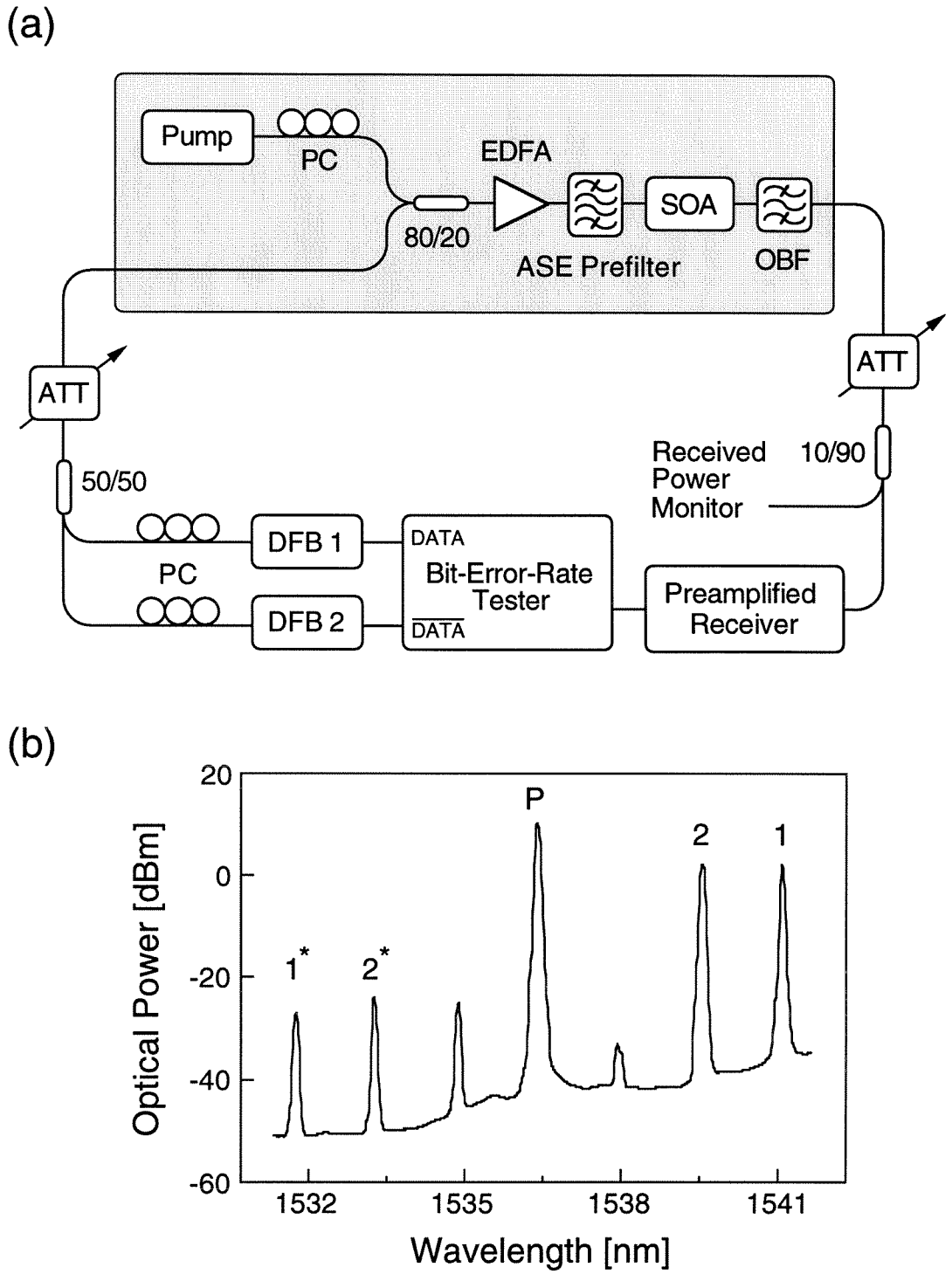

Figure 6.1: (a) A schematic of the experimental setup. (b) Optical spectrum measured into a 0.1 nm resolution bandwidth at the output of the SOA. The spectrum shows the two input channels 1 and 2, their respective converted signals 1* and 2*, and the pump P.

two independent signals at the input of the SOA. To study the penalty induced by crosstalk in 2-channel wavelength conversion, BER measurements are also made for a single-channel conversion using DFB1 alone for comparison. Measurements are made at various pump-to-signal power ratios of each individual channel at the output of the SOA (simply referred to as p/s ratio). The minimum p/s ratio of 6 dB is limited by the output powers of the DFB lasers and the choice of bi-directional couplers used in the setup to optimize conversion efficiency and optical SNR of the converted signal.

Qualitatively, the effect of crosstalk by parasitic cross-gain modulation can be easily seen in the eye diagrams. In Fig. 6.2 are shown two eye diagrams for small (a) and large (b) p/s ratios. For a small p/s ratio, the modulated power of the signal is a large portion of the total optical power in the SOA and therefore cross-gain saturation effects on the pump are significant. The eye diagram for $p/s = 8$ dB shows two distinct levels for a '1' bit; the higher level corresponding to when the other channel (in this case, DFB2) is a '0' bit and the lower level resulting from a decrease in the conversion efficiency due to the compression of the pump gain when the other channel is a '1' bit. The two levels are very distinct at small p/s ratios and merge for sufficiently large p/s ratios where the modulated power in the SOA becomes less significant.

Quantitatively, the effects of crosstalk can be seen in the bit-error-rate vs. received power curves shown in Fig. 6.3. Representative curves for PRBS 2^7-1 of the following cases are shown: 1-channel conversion with DFB1 and 2-channel conversion with DFB1 and DFB2. For the largest p/s ratio of 18 dB (open symbols), there is only a

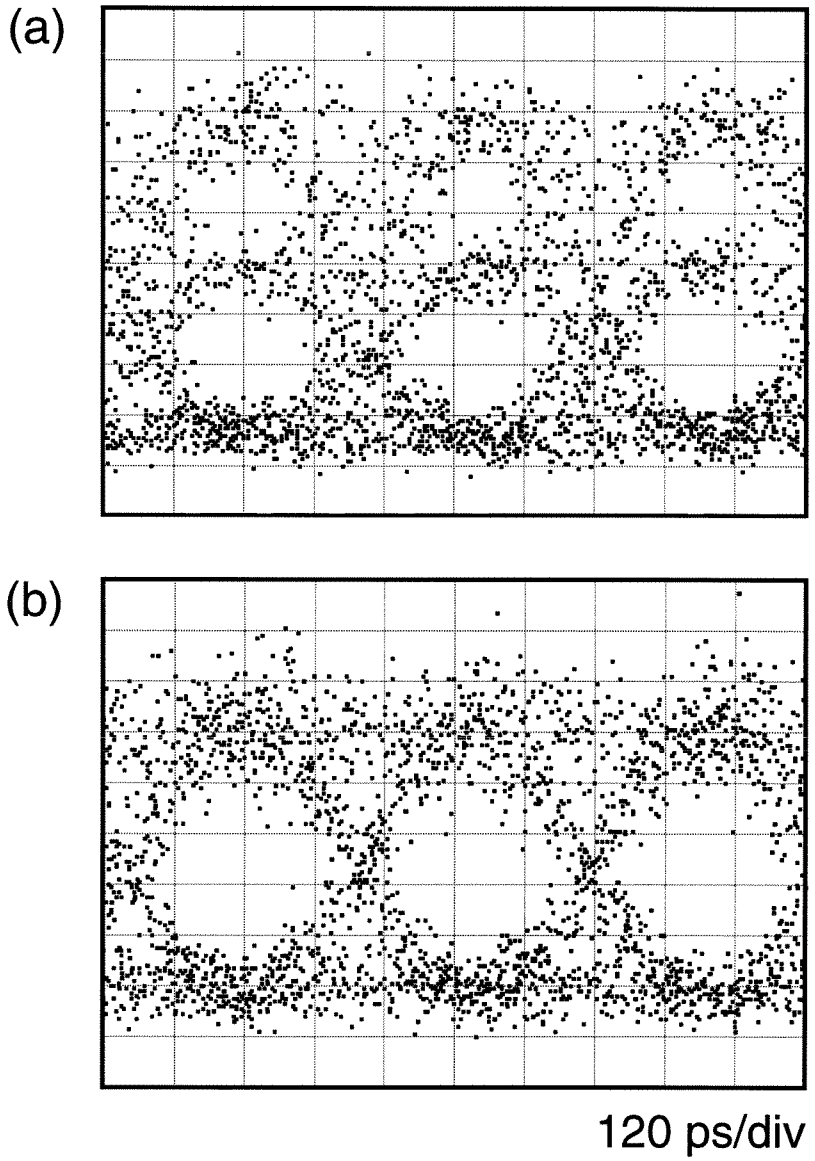

Figure 6.2: Eye diagrams showing the eye closure due to the parasitic cross-gain modulation in 2-channel wavelength conversion. Two limiting cases in pump-to-signal power ratios are shown. (a) $p/s = 8$ dB, (b) $p/s = 18$ dB.

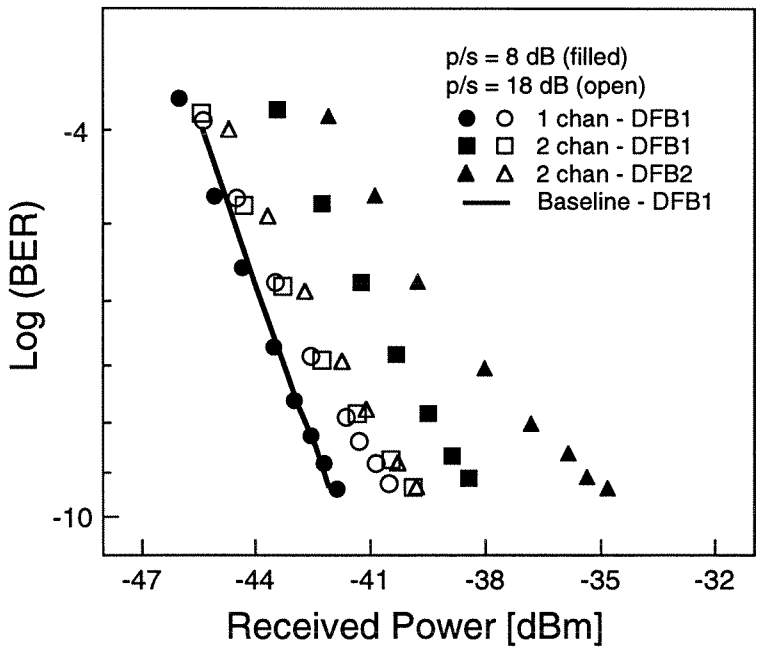

Figure 6.3: Bit-error-rate vs. received power for 1-channel and 2-channel wavelength conversion at 2.5 Gb/s for PRBS of length $2^7 - 1$. Representative curves are shown for $p/s = 8$ and 18 dB. A baseline is also shown for DFB1.

slight difference among the three cases. However, for the smallest p/s ratio of 8 dB, the difference between 1 and 2-channel conversion is significant and the penalty for the 2-channel conversion is as large as 6 dB compared to that of a single-channel conversion.

To summarize the effect of crosstalk on the system performance, Fig. 6.4 plots the receiver sensitivity for the above cases as a function of p/s ratio for both PRBS $2^7 - 1$ and $2^{31} - 1$. A significant penalty of > 6 dB is measured for 2-channel wavelength conversion at the lowest p/s ratio of 6 dB compared to the case of single-channel

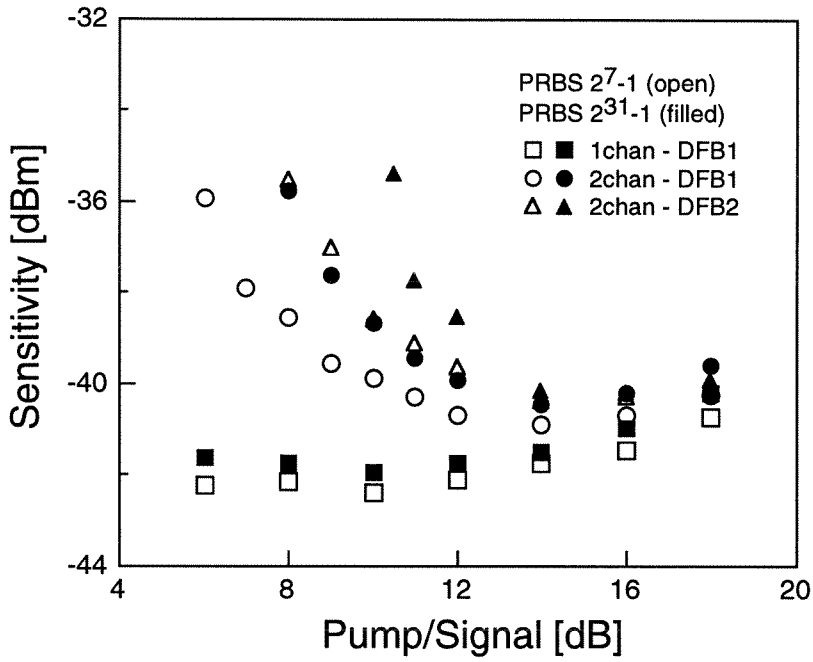

Figure 6.4: Receiver sensitivity (BER = 10^{-9}) vs. pump-to-signal power ratio for 1-channel and 2-channel wavelength conversion at 2.5 Gb/s. Pattern length dependence is also shown for PRBS $2^7 - 1$ and $2^{31} - 1$.

conversion. At higher p/s ratios ($\geq$ 15 dB), the 2-channel and 1-channel sensitivities parallel each other and the difference for all cases is $<$ 2 dB. The significant penalty we measure is consistent with the results presented in Ref. [2], as the p/s ratio in that work is greater than 15 dB. The difference in performance of DFB1 and DFB2 in 2-channel conversion is partly a result of the inferior performance of DFB2 even in the case of a single-channel conversion.

6.3 Discussion

For a single-channel conversion, the sensitivity degrades by only 1.5 dB over the range of p/s ratios and the pattern length dependence is small ($\leq$ 0.5 dB). For $p/s \leq 15$ dB, the converter performance, as quantified by the receiver sensitivity, is relatively constant demonstrating a dynamic range of input signal power of approximately 10 dB. To assess the sources of penalty, a simple model for the preamplified receiver is used to calculate BER. The model takes into account the slight variation in the gain of the EDFA preamplifier as a function of input power. For the single-channel conversion, the model predicts a degradation in sensitivity of 2.0 dB for the range of experimental p/s ratios, in good agreement with the experimental results. This degradation results from the reduction in the optical SNR of the converted signal with increasing p/s ratio. The pump-to-signal ratio at which measurable penalty occurs is a function of the conversion efficiency and the ASE noise in the optical bandwidth of the converted signal in the SOA, or equivalently the optical SNR. For an SOA converter of higher efficiency in combination with ASE noise prefiltering, the sensitivity will remain flat to a greater value of p/s ratio.

For the 2-channel conversion, there is a further degradation in the sensitivity resulting from at least three mechanisms. First, because the gain of the EDFA in the wavelength converter is saturated, the power in the additional channel reduces the pump power resulting in a decrease in the conversion efficiency and the optical SNR of the converted signal. This results in $\sim$0.3 dB degradation in sensitivity for the complete range of p/s values. Second, additional penalty results from the cross-gain

modulation of the pump by the signal channels in the SOA. The lower level for the '1' bit seen in the eye diagrams induces penalty because there is less power at the '1' level given the same average received power into the receiver. The compression of the '1' level to ~60 % at $p/s = 8$ dB is consistent with the measured cross-gain modulation on the pump. Finally, the presence of a second channel also induces additional noise, *i.e.*, the noise power on the converted signal is enhanced when there is power in the second channel. The mechanism by which this occurs has also been verified experimentally as being due to cross-gain saturation. In a similar experiment using a mixed-strained SOA for polarization independent gain, we have measured the additional noise power on the pump and the converted signal in the presence of the second channel, both for parallel and perpendicular polarization states to the first channel. The noise power enhancement in the converted signal is measured to be a factor of ~1.8 for $p/s = 8$ dB at both polarization states. Based on this empirical data, the model predicts a penalty of 5.7 dB above that of a single-channel conversion at $p/s = 8$ dB, which is in good agreement with the experimental data. The above three mechanisms have been identified as contributing factors to the additional penalty seen for 2-channel wavelength conversion. The pattern length dependence in the case of 2-channel conversion is accentuated due to the intersymbol interference (ISI) between the two channels.

In conclusion, we have measured the adverse effects of crosstalk by cross-gain saturation on the BER performance of simultaneous 2-channel wavelength conversion by FWM in a semiconductor optical amplifier. The receiver sensitivity degradation

has been quantified for two 2.5 Gb/s ASK channels wavelength converted by 6 and 9 nm. For large pump-to-signal power ratios ($\geq$ 15 dB), the 2-channel conversion performance is similar to that of the single-channel conversion. However, for small pump-to-signal power ratios ($\sim$ 8 dB), a significant penalty of up to 6 dB compared to that of a single-channel conversion is observed.

Bibliography

[1] R. Schnabel, U. Hilbk, Th. Hermes, P. Meißner, Cv. Helmolt, K. Magari, R. Raub, W. Pieper, F. J. Westphal, R. Ludwig, L. Küller and H. G. Weber, "Polarization insensitive frequency conversion of a 10-channel OFDM signal using four-wave-mixing in a semiconductor laser amplifier," *IEEE Photon. Technol. Lett.*, vol. 6, pp. 56–58, 1994.

[2] J. P. R. Lacey, S. J. Madden, M. A. Summerfield, R. S. Tucker and A. I. Faris, "Four-channel WDM optical phase conjugator using four-wave mixing in a single semiconductor optical amplifier," *Electron. Lett.*, vol. 31, pp. 743–744, 1995.

[3] K. Inoue, T. Hasegawa, K. Oda and H. Toba, "Multichannel frequency conversion experiment using fibre four-wave mixing," *Electron. Lett.*, vol. 29, pp. 1708–1710, 1993.

[4] S. J. B. Yoo, A. Rajhel, C. Caneau, R. Bhat and M. A. Koza, "Multichannel polarization-independent wavelength conversion by difference-frequency generation in AlGaAs waveguides," *Optical Communication Conference 1997*, Dallas, Texas, paper TuO6.

[5] Robert B. Lee, David F. Geraghty, Per Olof Hedekvist and Kerry J. Vahala, "Crosstalk penalty in 2-channel wavelength conversion by four-wave mixing in a strained semiconductor optical amplifier," *Optical Fiber Communication Conference 1997*, Dallas, Texas, poster WL53.

Chapter 7

Dispersion Compensation

7.1 Introduction

The chromatic dispersion of standard single-mode silica fiber (zero dispersion at 1.3 μm) is approximately 17 ps/nm/km placing a severe limit on the maximum transmission distance for high bit-rate systems operating at 1.55 μm. In recent years, dispersion compensation techniques have been developed to enable high bit-rate transmission over installed fiber links comprising mostly of standard dispersion fiber. The various techniques include prechirping by current injection into the laser diode signal source of an externally modulated system [1], by reflection from a chirped fiber bragg grating [2] and by transmission in fiber bragg grating outside the reflection band [3]. Periodic use of dispersion compensating fiber with negative dispersion slope has also been used to manage dispersion [4]. Optical phase conjugation (spectral inversion) by four-wave mixing also provides a mechanism for achieving dispersion compensation as first proposed by Yariv *et al.*, in 1978 [5].

In this chapter, spectral inversion in wavelength conversion by four-wave mixing in a semiconductor optical amplifier is evaluated using a time-resolved spectral analysis technique. Multiple patterns are examined before and after undergoing wavelength conversion [6]. The resulting spectral inversion is then applied toward dispersion compensation of a directly-modulated DFB laser signal at 10 Gb/s by mid-span spectral inversion in an unrepeatered 120 km transmission in dispersive fiber.

7.2 Time-Resolved Spectral Analysis

In a semiconductor gain medium, optical intensity modulation changes the carrier density inducing both gain and refractive index modulation. As a result, the wavelength of the optical wave passing through the device becomes chirped. The impact of the chirp resulting from wavelength conversion techniques based on cross-gain modulation in an SOA [7] and in tunable semiconductor laser [8] on transmission in fiber has been studied previously. However, no direct measurements of the chirp induced from the wavelength conversion process based on four-wave mixing in a semiconductor optical amplifier have been made. Here we use time-resolved spectral analysis (TRSA) [9] to evaluate the chirp of a directly-modulated DFB laser at 10 Gb/s before and after wavelength conversion.

The experimental setup is shown in Fig. 7.1. A 10 Gb/s non-return-to-zero pattern is used to directly modulate a DFB laser. For the unconverted signal, the output of the DFB laser is passed through a narrow bandpass filter (a Hewlett-Packard optical spectrum analyzer (OSA) with optional monochromator output) and detected using

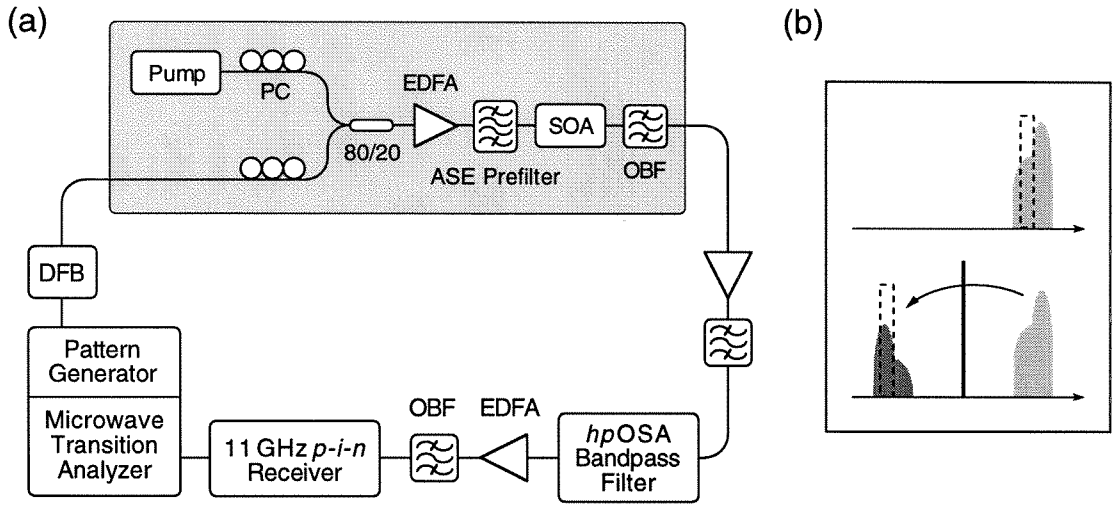

Figure 7.1: (a) Experimental setup for time-resolved spectral analysis of the spectral inversion resulting from four-wave mixing in a semiconductor optical amplifier. (b) Illustration of the chirped spectrum and the narrowband filter for unconverted and converted signals.

a 11 GHz DC-coupled *p-i-n* receiver after amplification by an EDFA-OBF pair. The chirped spectrum of a directly-modulated DFB laser and the filter are illustrated in top portion of Fig. 7.1(b). The OSA provides an accurately-tunable filter of 0.08 nm bandwidth that is stepped across the spectrum at 0.005 nm increments. The resulting pattern from a spectral slice is analyzed by a microwave transition analyzer with a temporal resolution of $\sim$3 ps. Typically up to 120 spectral slices across a chirped spectrum are compiled creating a map of the spectral power distribution as a function of time. The identical procedure is then applied to the signal wavelength converted by 6 nm as illustrated in Figs. 7.1(a) and (b). The measurements are repeated for

several different 8 bit patterns.

The results for the 1001 1100 pattern are summarized in Fig. 7.2. The top panel shows the 10 Gb/s intensity pattern of the input signal. The bottom panel shows the average wavelength as a function of time for the input signal and the converted signals for pump-to-signal power ratios of 3 and 9 dB. The wavelength chirp is most significant on the rising and falling edges of the intensity pattern where carrier density changes most rapidly in the DFB laser. Qualitatively, the spectral inversion of the wavelength conversion process, *i.e.*, the reflection of the wavelength chirp about a horizontal line, is easily seen.

Quantitatively, the wavelength chirp increases from 1.2 Å before to 1.7 Å after the wavelength conversion for the $p/s = 3$ dB case. The modulated optical power is ~50 % of the total maximum power in the SOA and thus significant additional chirp is induced in the conversion process. For the $p/s = 9$ dB case where the modulated optical input power is only a small fraction of the total power, although there is no measurable overall chirp increase, there are nonetheless small distortions to the spectral inversion. The distortions can be minimized by further increasing the p/s ratio, however, ~9 dB is a practical limit in order to achieve satisfactory BER performance after wavelength conversion. For patterns ranging from an isolated 1 followed by seven 0's to its complement, the increase in the total chirp is 6–44 %.

In this section, we have utilized time-resolved spectral analysis to measure the spectral inversion properties of wavelength conversion by FWM in an SOA. The wavelength chirp is approximately reversed by the conversion process, however, due

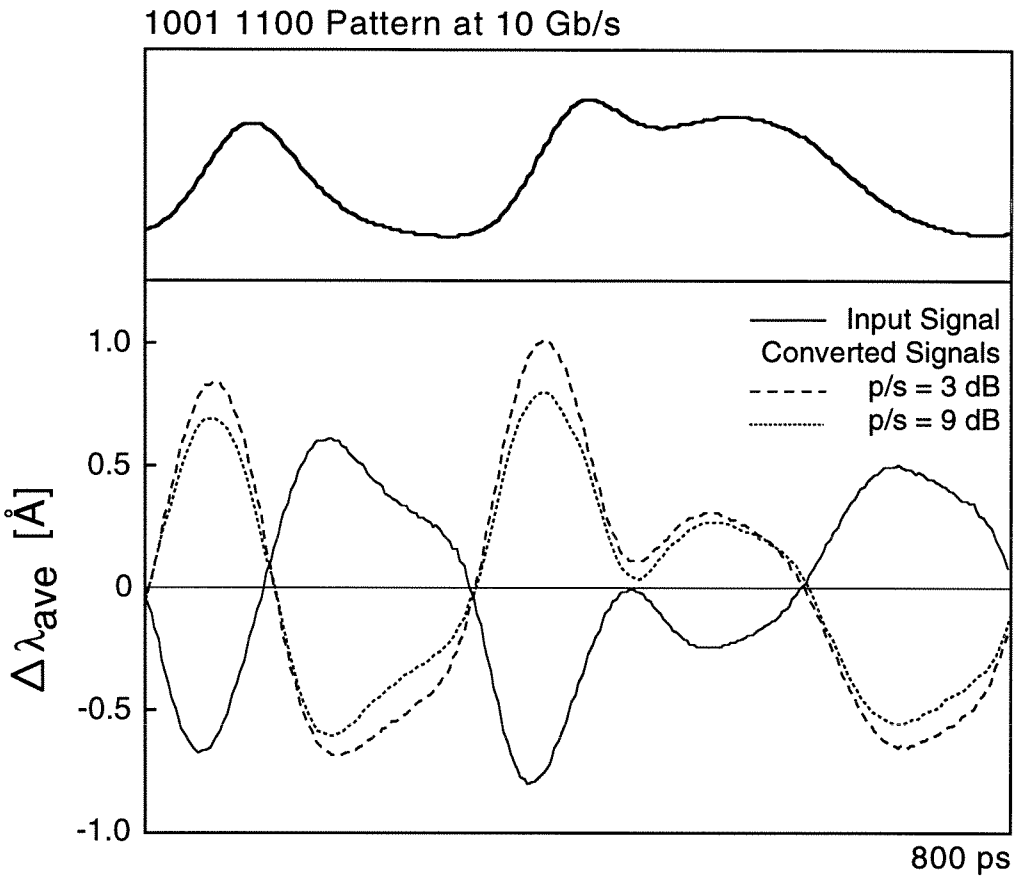

Figure 7.2: The top panel shows the complete bit pattern of 1001 1100. The bottom panel shows the average wavelength as a function of time for the unconverted and the converted signals for pump-to-signal power ratios of 3 and 9 dB. For the 3 dB case, a significant increase in wavelength chirp is measured.

to the gain and phase modulation in the SOA from the modulated input signal, the overall chirp is increased.

7.3 Dispersion Compensation by Mid-Span Spectral Inversion

In a typical directly-modulated DFB laser source, the wavelength shifts to the blue (shorter wavelength) on the rising edge and to the red (longer wavelength) on the falling edge. This is in fact the case for the DFB laser used in the experiment as measured in the previous section (Fig. 7.2). Operating at 1.55 μm in the region of anamolous dispersion ($\beta'' = \frac{d^2\beta}{d\omega^2} < 0$) for a dispersive single-mode fiber (SMF), the shorter wavelength travels faster thus broadening the pulse by propagation. However, for a reversed chirp, *i.e.*, wavelength shift to the red on the rising edge and to the blue on the falling edge, the group velocity dispersion of the fiber would compress the pulse. Therefore, by chirp reversal resulting from optical phase conjugation at the midpoint of the transmission link, the chromatic dispersion is compensated for and the pattern is regenerated to its original shape. The second order dispersion does, however, remain uncompensated. The above technique of compensation by mid-span spectral inversion (MSSI) has been demonstrated using four-wave mixing in dispersion shifted fibers by Watanabe *et al.* [10], and in a semiconductor optical amplifier by Tatham *et al.*, at 10 Gb/s for a directly-modulated DFB laser [11].

In this section we illustrate how mid-span spectral inversion can be used to achieve 120 km transmission of a directly-modulated DFB at 10 Gb/s. The experimental

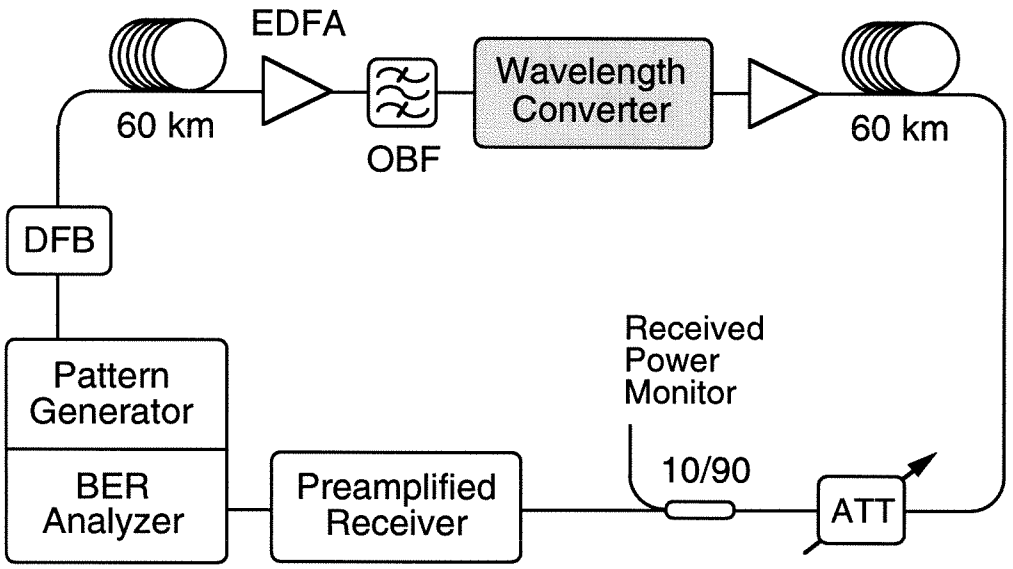

Figure 7.3: Experimental setup for dispersion compensation by mid-span spectral inversion for two transmission segments of 60 km.

setup is shown in Fig. 7.3. The directly-modulated DFB signal is transmitted through 60 km of dispersive SMF and amplified to compensate for the propagation losses. Following wavelength conversion, the converted signal is amplified and launched through an identical 60 km of SMF. The pump-to-signal power ratio is set to 9 dB to minimize distortions to the spectral inversion process.

In Fig. 7.4 are shown the eye diagrams for PRBS $2^7 - 1$ and the 1001 1100 pattern at various stages of 120 km transmission. After 60 km transmission, both the eye diagram and the pattern have significantly degraded. After 120 km transmission without any compensation, the eye diagram is completely obliterated and the iso-

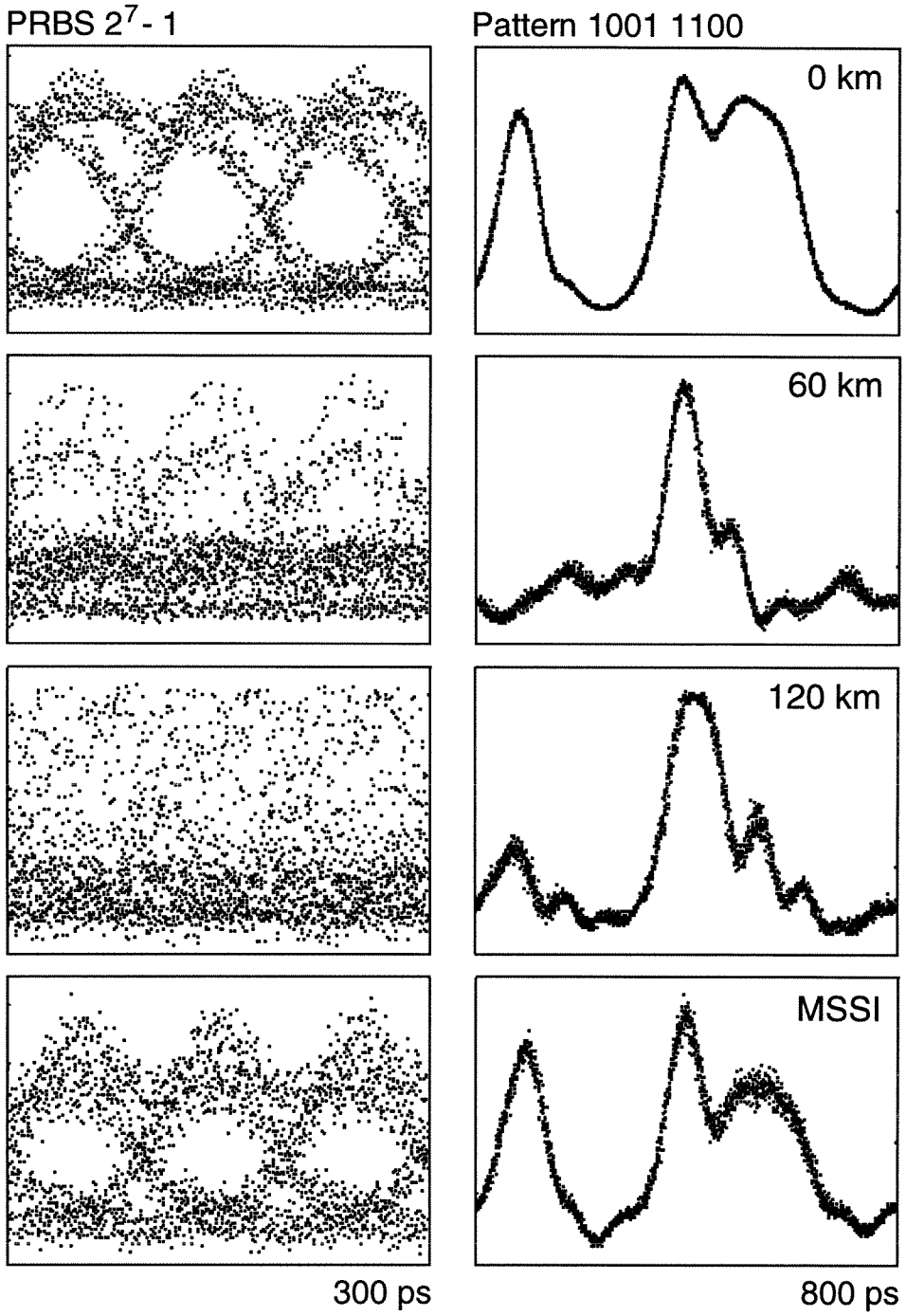

Figure 7.4: Eye diagrams of PRBS $2^7 - 1$ and pattern 1001 1100 at 10 Gb/s for 0, 60 and 120 km transmission without compensation and 120 km transmission with compensation by mid-span spectral inversion.

lated '1' bit in the 8 bit pattern has essentially disappeared. However, for 120 km transmission with MSSI, the open eye diagram and the general shape of the 8 bit pattern are recovered. The pattern regeneration, however, is not perfect compared to that measured at 0 km transmission. This results mainly from the imperfect spectral inversion of the wavelength converter as measured in the previous section, and from the fact that the converted signal wavelength (λ_c) is different from the input signal wavelength (λ_s) thus the group velocity dispersion $\beta''(\lambda_s) \neq \beta''(\lambda_c)$. For an ideal spectral inversion, however, compensation can be optimized by satisfying the relationship $\beta''(\lambda_s)L_1 = \beta''(\lambda_c)L_2$ where $L_{1,2}$ are the lengths of the fiber segment before and after spectral inversion, respectively [5].

The BER performance is measured on the regenerated PRBS $2^7 - 1$ pattern after 120 km transmission by MSSI. A penalty of 3.5 dB is measured relative to the BER performance after wavelength conversion without any transmission in dispersive fiber.

Bibliography

[1] N. Henmi, T. Saito and T. Ishida, "Prechirp technique as a linear dispersion compensation for ultrahigh-speed long-span intensity modulation direct detection optical communication-system," *J. Lightwave Technol.*, vol. 12, pp. 1706–1719, 1994.

[2] R. I. Laming, W. H. Loh, X. Gu, M. N. Zervas, M. J. Cole and A. D. Ellis, "Dispersion compensation with chirped fiber bragg grating to 400 km at 10 Gbit/s in nondispersion-shifted fiber," *Optical Fiber Communication Conference 1996*, San Jose, California, paper ThA5.

[3] K. O. Hill *et al.*, "Chirped in-fiber bragg gratings for compensation of optical-fiber dispersion," *Optics Lett.*, vol. 19, pp. 1314-1316, 1994.

[4] R. J. Nuyts, Y. K. Park and P. Gallion, "Dispersion equalization of a 10 Gb/s repeatered transmission-system using dispersion compensating fibers," *J. Lightwave Technol.*, vol. 15, pp. 31–42, 1997.

[5] A. Yariv, D. Fekete and D. M. Pepper, "Compensation for channel dispersion by nonlinear optical phase conjugation," *Optics Lett.*, vol. 4, pp. 52–54, 1979.

[6] David F. Geraghty, Robert B. Lee and Kerry J. Vahala, "Time-resolved spectral analysis of phase conjugation by four-wave mixing in a semiconductor optical amplifier," *Conference on Lasers and Electro-Optics 1997*, Baltimore, Maryland, paper CTuH.

[7] K. Inoue, "Dependence of chirping influence on probe input power in wavelength conversion based on cross-gain saturation in a semiconductor optical amplifier," *Electron. Lett.*, vol. 32, pp. 584–585, 1996.

[8] H. Sanjoh, H. Mawatari, H. Ishiii, H. Yasaya, Y. Yoshikuni and K. Oe, "Wavelength chirping in wavelength conversion of 10 Gb/s signal with semiconductor laser converter," *IEEE Photon. Technol. Lett.*, vol. 8, pp. 296–298, 1996.

[9] R. A. Linke, "Modulation induced transient chirping in single frequency lasers," *IEEE J. Quantum Electron.*, vol. QE-21, pp. 593–597, 1985.

[10] S. Watanabe, T. Naito and T. Chikama, "Compensation of chromatic dispersion in a single-mode fiber by optical-phase conjugation," *IEEE Photon. Technol. Lett.*, vol. 5, pp. 92–95, 1993.

[11] M. C. Tatham, X. Gu, L. D. Westbrook, G. Sherlock and D. M. Spirit, "Transmission of 10 Gbit/s directly modulated DFB signals over 200km standard fibre using mid-span spectral inversion," *Electron. Lett.*, vol. 30, pp. 1335–1336, 1994.

Chapter 8

Formation of Highly-Uniform and Densely-Packed Arrays of GaAs Dots by Selective Epitaxy

8.1 Introduction

Semiconductor diode lasers are the key components at the center of many consumer technologies, *e.g.*, compact disc players, laser printers and fiber optic communication systems. The continued research on these devices is not only motivated by their technological importance, but by the ability to study new interesting phenomena. This is especially true in the case of quantum well lasers.

The modern double heterostructure semiconductor lasers in which higher bandgap semiconductor material provides a potential well confinement for the electrons and holes in the active layer of the laser were proposed in 1963 [1][2]. In the early 1970's

scientists contemplated what might happen when these confined active layers became extremely thin. With the advent of crystal-growth techniques such as molecular-beam epitaxy (MBE) and organometallic vapor-phase epitaxy (OMVPE), with atomic-scale compositional control along the growth direction, it became possible to fabricate structures with active layers on the order of 100 Å in thickness exhibiting quantum-confinement effects. The benefits of such devices, referred to as quantum well lasers, can be understood by examining the density of states as illustrated in Fig. 8.1. In a bulk semiconductor, the density of states increases as the square root of the energy, however, in quantum wells, the increase is step-like. High gain requires population inversion of energy levels with a high density of states. In a bulk laser, this condition can be achieved only after filling the lower lying energy states. However this is unnecessary in a quantum well laser, and results in a lower threshold current and higher differential gain. Other advantages include lower internal loss, higher modulation bandwidth and lower chirp.

The natural extension of quantum well lasers is to develop technologies which would enable equivalent control in the lateral directions perpendicular to the growth direction. Such a capability would greatly enhance the possible structures that can be fabricated, in particular, quantum wires and dots, structures of quantum confinement in two and three dimensions, respectively. These structures have attracted considerable attention for their potential in improving optoelectronic devices. Their incorporation into the active layer of a laser diode have been predicted to provide significant improvement in performance [3][4]. The further narrowing of the density

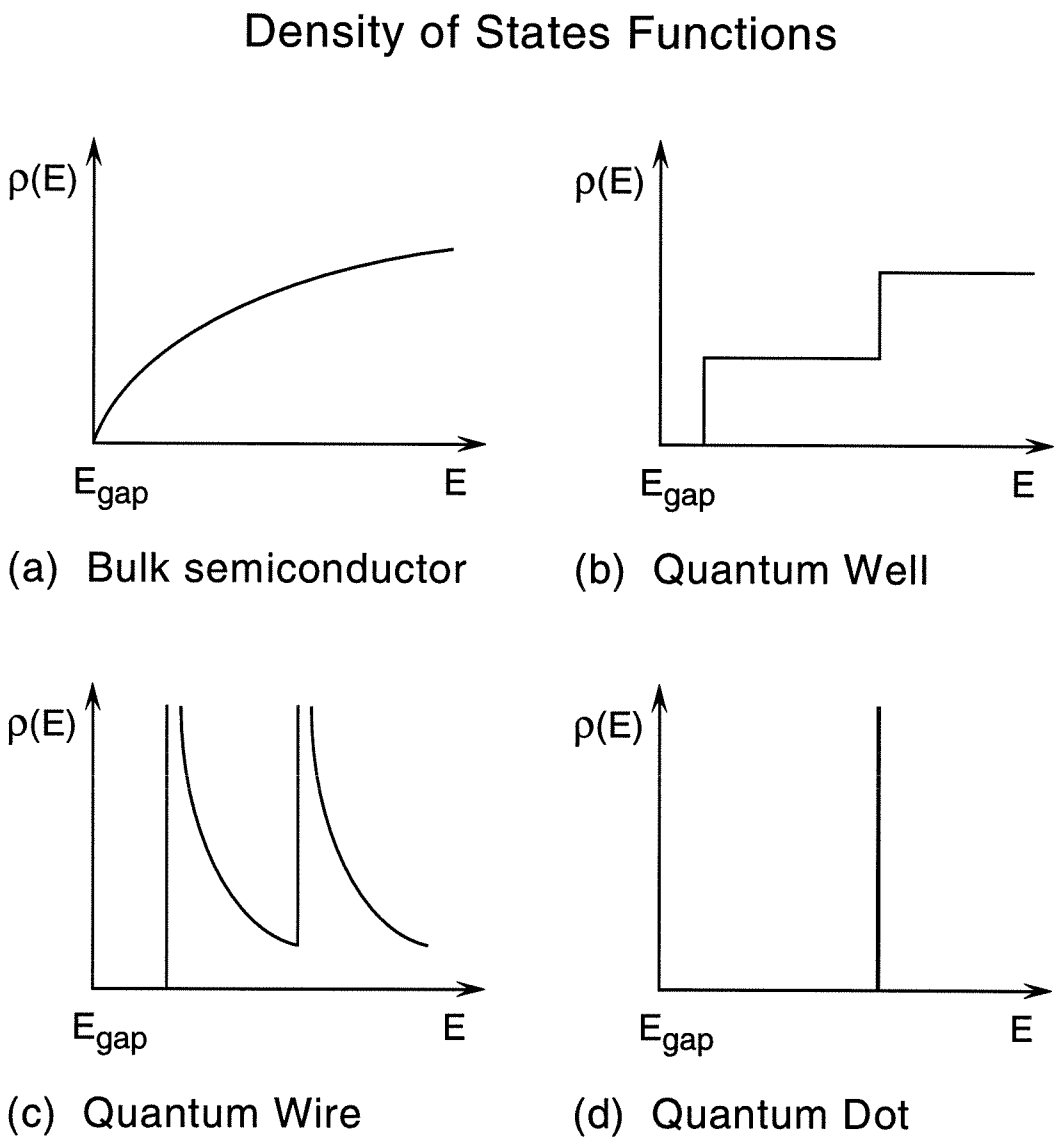

Figure 8.1: The density of states functions for (a) bulk semiconductor material, (b) quantum well, (c) quantum wire and (d) quantum dot.

of states function with increasing quantum confinement as illustrated in Fig. 8.1(c) and (d) result in reduced threshold currents and linewidths for laser diodes based on quantum wires or dots.

A variety of approaches for fabrication of such nanostructures have been studied: lithographic patterning of an existing quantum well structure [5][6], impurity-induced disordering using ion-beam implantation [7] and strained-induced island formation [8][9]. The first two techniques suffer from damaged surfaces or lack of interface control, and the third technique is limited to appropriately strained material systems. Selective epitaxy, which refers to the laterally controlled growth of epitaxial material within openings of a masking material has also produced promising results. In particular, highly-organized dot structures exhibiting excellent uniformity and good luminescence efficiency have been formed by selective epitaxy [10]–[12].

In this chapter, the formation of highly-uniform and densely-packed arrays of GaAs dots by selective epitaxy using diethylgallium chloride and arsine is described. The arrays of GaAs dots as small as 15–20 nm in base diameter and 8–10 nm in height are characterized using contact-mode atomic force microscopy [13].

8.2 Organometallic Vapor-Phase Epitaxy

The technique utilized for the fabrication of nanometer-scale structures in GaAs is selective organometallic vapor-phase epitaxy (OMVPE). The OMVPE reactor used in the experiment is briefly described in this section along with a description of the selective OMVPE chemistry.

8.2.1 OMVPE Reactor Configuration

The OMVPE reactor system used in the experiment is an AIXTRON 200/4 located in the Microdevices Laboratory (MDL) of the NASA Jet Propulsion Laboratory (JPL). The basic modules comprising the reactor system are shown schematically in Fig. 8.2. Although complex, the reactor system can be partitioned into several basic modules: computer control module with digital and analog controls, carrier and hydride gas and organometallic source handling, the deposition chamber, and the exhaust treatment.

The computer control module is a windows-based graphical environment. Due to the complexity and the number of flow and pressure control elements, an integrated control system is critical to the operation of the reactor. This control environment also provides in software and hardware safety logic to prevent accidental injury to the operator, *e.g.*, an interlock preventing the opening of the deposition chamber without purging the chamber with nitrogen.

In the gas and source handling section, the carrier and hydride gases, and the organometallic (OM) materials are mixed together in the gas switching manifold. The H_2 carrier gas, purified by a heated palladium diffusion cell, is used to transport the organometallic vapors. The hydride source for GaAs is a 50:50::AsH_3:H_2. The precision control by use of mass flow controllers and properly designed gas manifolds allows the ability to make abrupt compositional shifts.

In the deposition chamber, a substrate is placed on a graphite susceptor which is heated by infrared lamps to temperatures of up to 800°C. The small amounts of OM material and hydride gases in the carrier gas decompose thermally and deposit

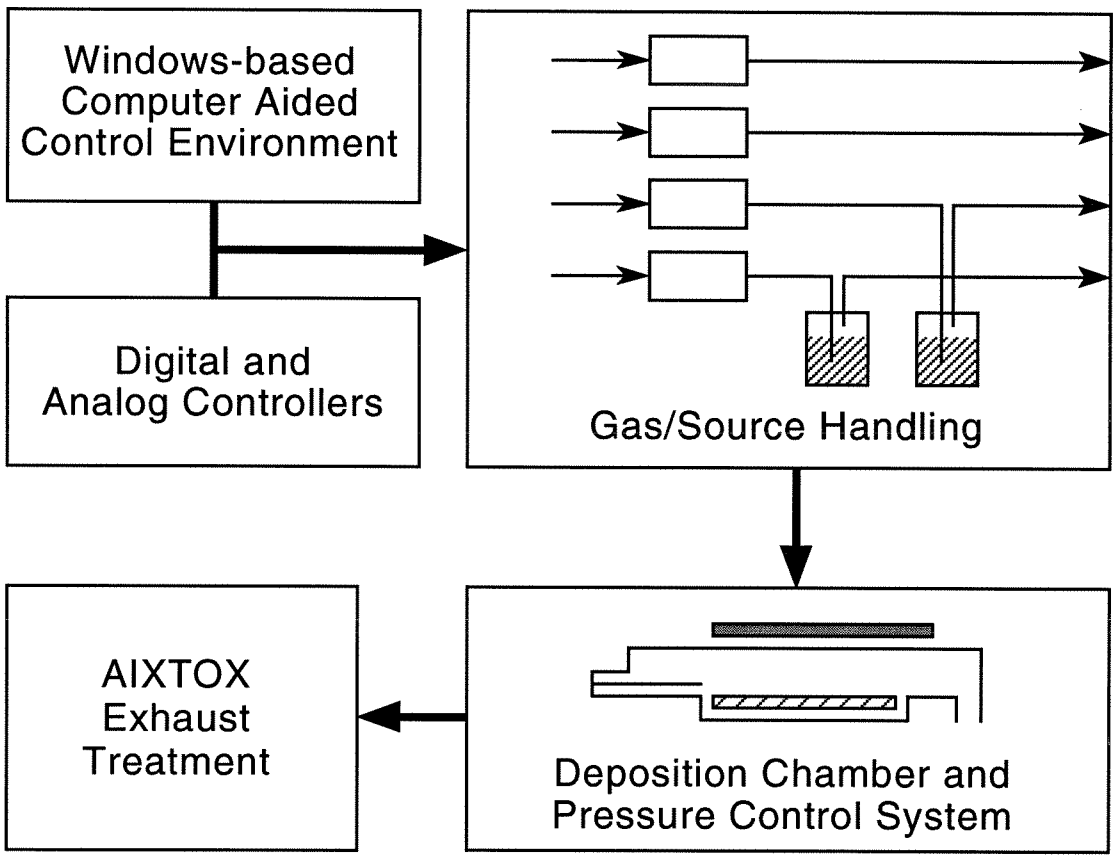

Figure 8.2: Schematic of the basic modules of the AIXTRON 200/4 OMVPE reactor system at the NASA Jet Propulsion Laboratory.

epitaxial layers on the substrate. The depleted gases and the solid byproducts of the gas-phase chemistry are then exhausted out of the chamber and filtered by the pressure control system.

The gaseous waste exhausted from the pressure control system must be treated due to the presence of acutely toxic gases such as AsH_3 and residual organometallic materials. In the AIXTOX scrubbing system, the exhaust gas stream is treated with an acidic solution of bromate or iodate salts. The hydride gases are oxidized into water-soluble acids. The treated gas stream of hydrogen is then exhausted by the main exhaust system of the building.

8.2.2 Selective OMVPE of GaAs

Selective epitaxy of GaAs, *i.e.*, the preferential deposition of epitaxial material within the mask openings, can be achieved in organometallic vapor-phase epitaxy using silicon nitride (Si_3N_4) or silicon dioxide (SiO_2) as the masking layer. Conventional OMVPE growth of GaAs uses trimethylgallium (TMGa) as the organometallic source and arsine (AsH_3) as the hydride source. In this chemistry, however, poor selectivity results. Typically polycrystalline material deposits over the dielectric-mask area in addition to the epitaxial deposition within the openings. The GaAs growth process for this chemistry, the complete reaction and the surface reaction, respectively, is as follows [14]:

$$\begin{aligned} (CH_3)_3Ga + AsH_3 &\Longrightarrow GaAs + 3\,CH_4 \\ CH_3Ga + AsH &\Longrightarrow GaAs + CH_4 \end{aligned} \tag{8.1}$$

The poor selectivity results from the surface reaction. There is no mechanism for the Ga atom to return to the gas phase once nucleation has taken place over the masked area.

The use of alternative halogen-based organometallic precursors such as diethyl-gallium-chloride (DEGaCl), however, have been shown to result in no deposition on the dielectric-mask area under appropriate conditions [15]. The complete reaction and the surface reaction for this process are as follows [16]:

$$\begin{aligned} (C_2H_5)_2GaCl + AsH_3 &\Longrightarrow GaAs + HCl + 2\,C_2H_6 \\ GaCl + AsH &\Longleftrightarrow GaAs + HCl \end{aligned} \tag{8.2}$$

The possible selectivity results from a reversible surface reaction. The GaAs deposition on the dielectric can be reversed under the appropriate conditions in the presence of HCl back into the gas phase of GaCl and AsH. This technique has been applied successfully previously in the fabrication of submicron wire and dot structures [15][16]. The selective chemistry using novel OM sources, provides a technique to achieve complete selectivity using a conventional OMVPE reactor for deposition of high-quality epitaxial structures.

8.3 Dot Formation by Selective Epitaxy

8.3.1 Fabrication Process

Using the selective OMVPE chemistry described, GaAs nanostructures are fabricated. A schematic illustrating the fabrication process is shown in Fig. 8.3. The substrates prepared for this study contained a 2 μm Si-doped $Al_{0.3}Ga_{0.7}As$ layer and a 10 nm undoped GaAs cap layer, both deposited by low-pressure OMVPE on Si-doped (100) GaAs substrates. A dielectric masking layer of silicon nitride was deposited by plama-enhanced chemical vapor deposition on the substrates and then annealed under an arsine ambient at typical OMVPE growth conditions. The thickness of the annealed silicon nitride layer was approximately 15 nm before lithographic patterning. A 40 μm $\times$ 40 μm arrays of dot openings with center-to-center spacings of 100 nm were patterned into the silicon nitride layer by high-resolution electron-beam lithography and reactive-ion etching in CF_4 plasma. The electron-beam dosages used for the lithography were varied to produce variations in the dot-opening sizes among 12 different arrays.

The growth of the arrays of GaAs dots were performed in an AIXTRON 200/4 OMVPE reactor. The growth precursors for organometallic-chloride (III) and the hydride (V) were diethylgallium-chloride (DEGaCl) and arsine (AsH_3), respectively. The DEGaCl bubbler temperature was maintained at 17°C and the vapor-phase V/III ratio was maintained at $>$ 100. The patterned samples were annealed under an AsH_3/H_2 ambient at the growth temperature of 700°C for 10 minutes prior to the actual growth and no dopants were intentionally introduced.

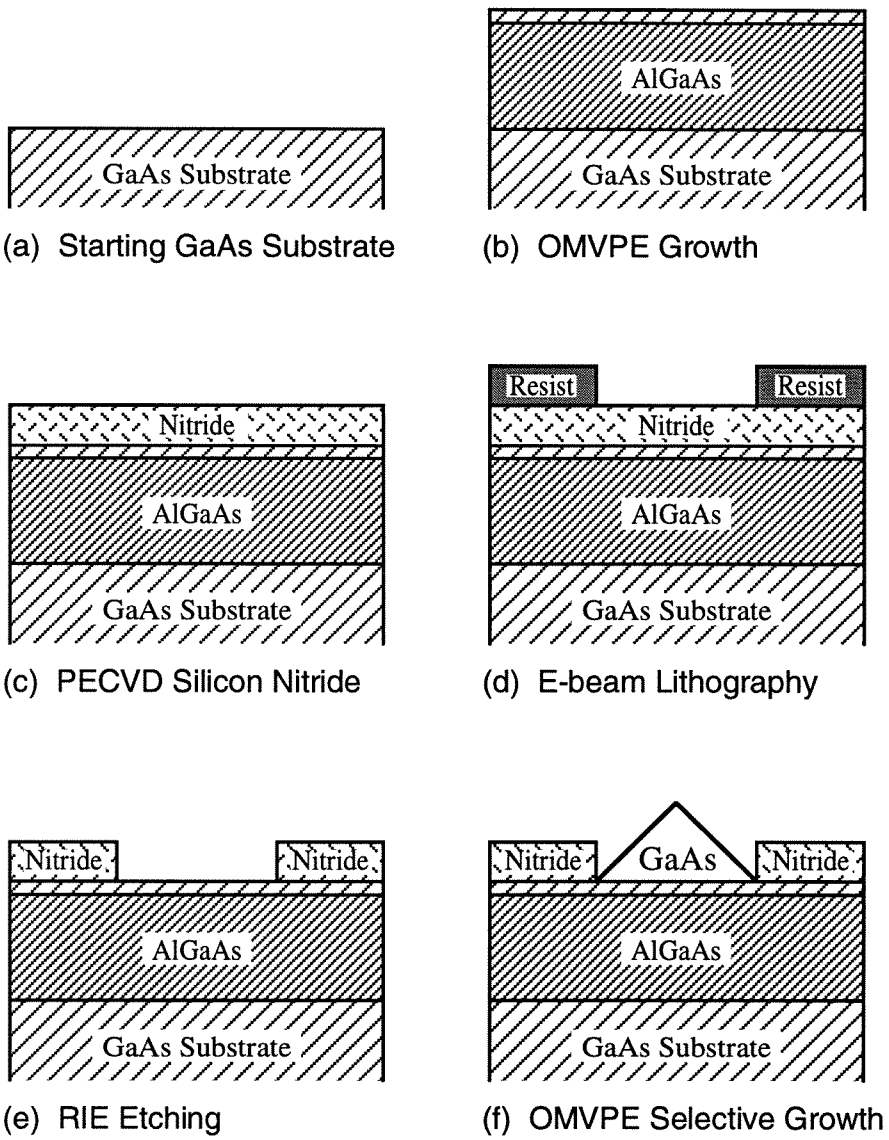

Figure 8.3: Schematic illustration of the basic fabrication procedure for selective dot growth.

8.3.2 Characterization and Analysis by Atomic Force Microscopy

The arrays of GaAs dots were imaged by contact-mode atomic force microscopy (AFM). The AFM operating parameters were optimized to image these small dot structures. The contact force chosen for the etch-sharpened silicon AFM probes was an empirical compromise between fast tip-wear and tip lift-off. For the AFM tip to closely track the surface features, the probe feedback gains were maximized and slow scan rates and small scan areas were used. Each AFM image took approximately 20 minutes to complete. The acquired AFM image data were plane-fitted to remove the effects of thermal drift and small tilt from the sample and/or the AFM. No other image processing procedures were applied to enhance the image data.

Plane views and three-dimensional views of the arrays of GaAs dots were generated using the AFM. Fig. 8.4 contains three plane-view AFM images of the GaAs dots from different arrays. The apparent sizes of the dots are: (a) 22 nm, (b) 35 nm and (c) 57 nm. Fig. 8.5 contains two three-dimensional view AFM images of the same arrays of GaAs dots corresponding to Figs. 8.4(b) and (c). These AFM images of the arrays of GaAs dots illustrate that the dots are highly uniform and densely packed within each array. By analyzing the AFM image data, the areas of individual dots within each array were determined. The normalized standard deviations of the areas of individual dots were 16 % for the array illustrated in Fig. 8.4(a), 10 % for the array in Fig. 8.4(b), 8 % for the array in Fig. 8.4(c) and 6 % for the arrays with the largest dots. In addition, these images confirm that the GaAs deposition is entirely selective under these growth conditions. No deposition occurred outside of the dielectric-mask

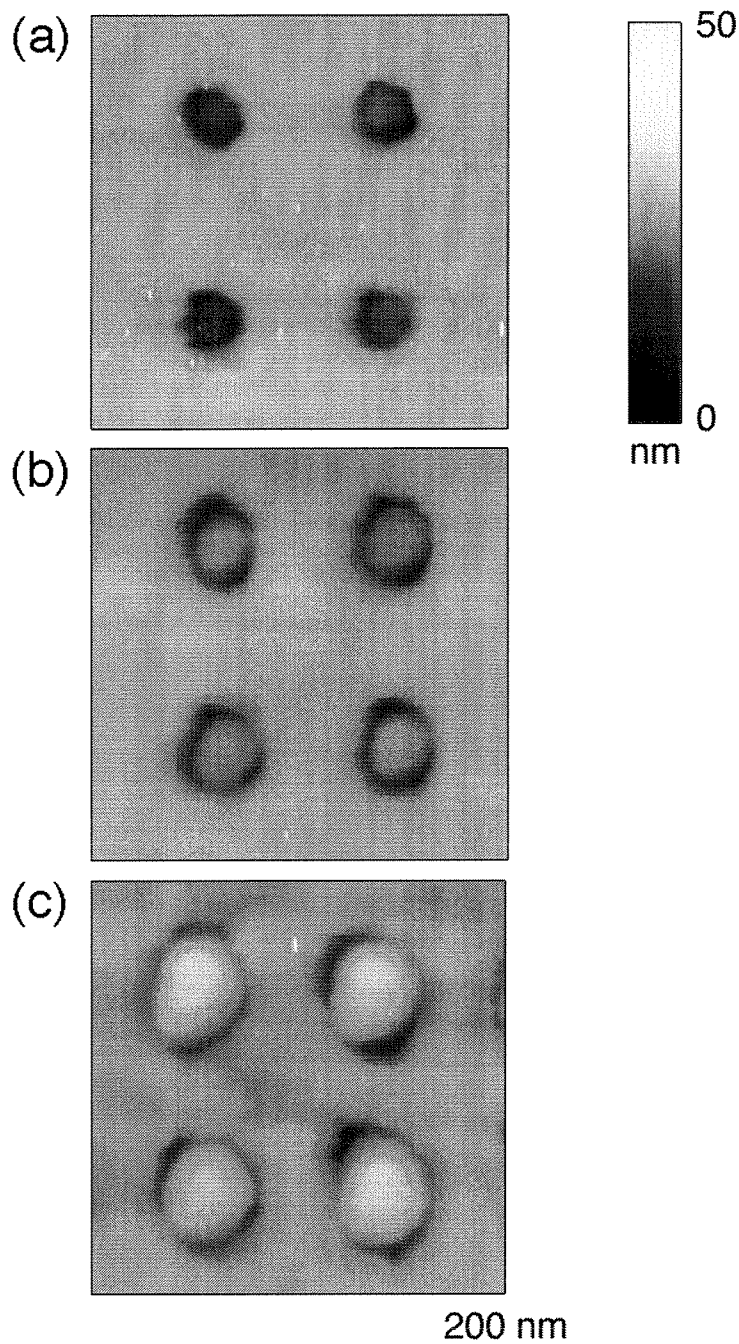

Figure 8.4: Atomic force micrographs in plane view of arrays of (a) small, (b) medium and (c) large GaAs dots after OMVPE growth. The scan area is 200 nm × 200 nm. The height is represented in grayscale. The dot center-to-center spacing is 100 nm.

openings.

After the initial AFM imaging, the samples were etched in a low-bias-voltage CF_4/O_2 plasma to remove the silicon-nitride layer. In Fig. 8.6 are shown two three-dimensional view AFM images of the arrays of GaAs dots after the removal of the silicon nitride. The arrays shown correspond to the arrays of Figs. 8.4(a) and (b). The apparent sizes of the dots are (a) 44 nm and (b) 55 nm. These images are noisier than the previous images. The possible reasons include chemical contamination resulting from the use of solvents to take the samples off the AFM mount, and uneven etching and/or surface roughening from the plasma etching process.

The height and the base diameter of the GaAs dots, with the silicon-nitride layer removed, were measured for the different arrays. The results are summarized in Fig. 8.7(a) along with the best-fit line. The x-intercept of the fit is not at zero base diameter, but at $\sim$29 nm. This results from the finite radius of curvature R of the AFM probe tip. In Fig. 8.7(b), its effect on the accurate imaging of small dot structures is illustrated. The x-intercept of the best-fit line at $\sim$29 nm agrees well with the manufacturer's specifications for the probe tip radius of curvature of 10–30 nm.

The slope of the best-fit line being $\sim$0.48 indicates that the growth of the dots is self-limited most likely by 45° planes or (110)-type crystal planes. The (110) planes have been identified as the slow-growth crystal planes previously for this growth process [15][16]. The experimental data, correcting for the limitations due to the AFM tip radius of curvature, indicate that the dots are as small as 15–20 nm in base

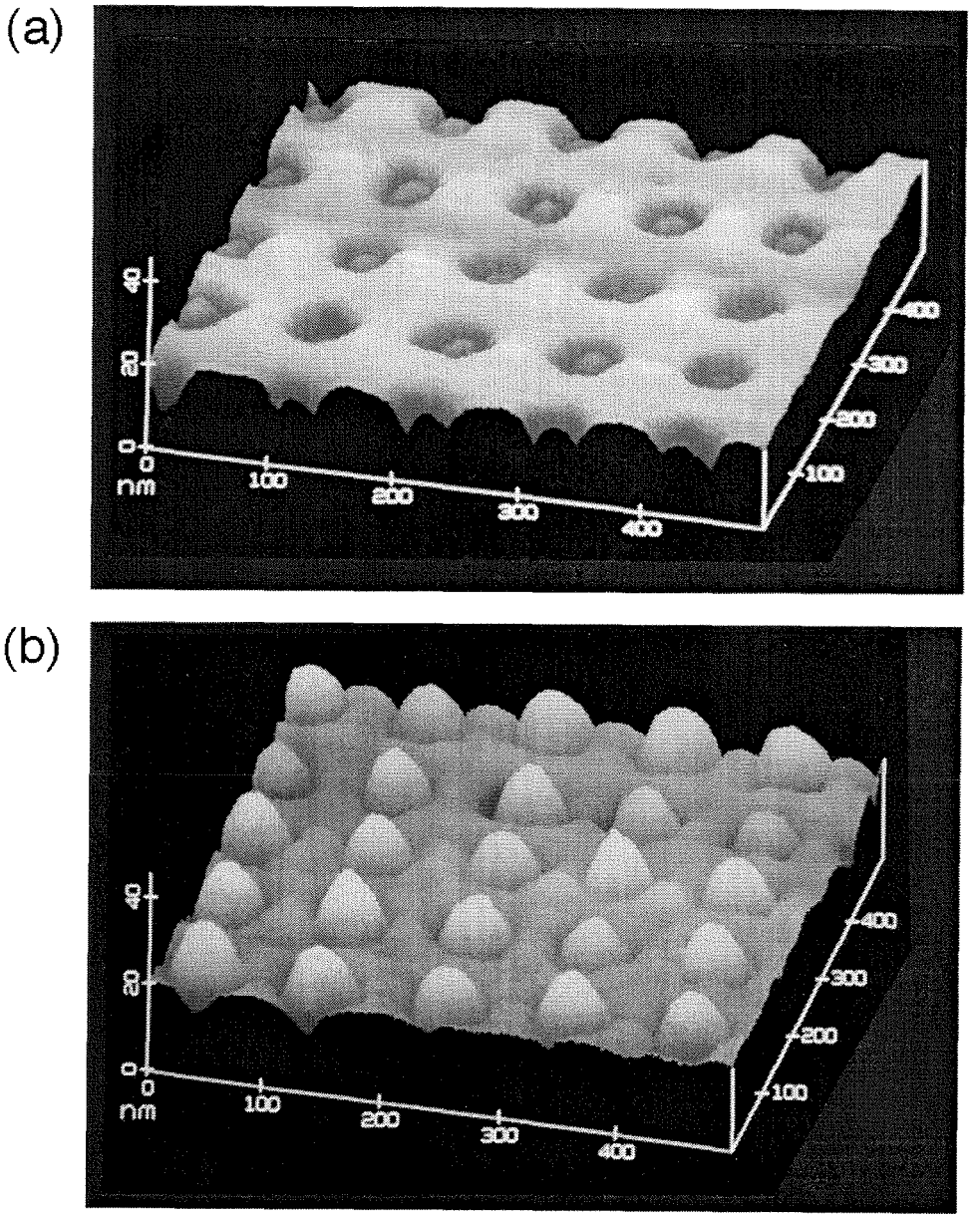

Figure 8.5: Atomic force micrographs in three-dimensional view of arrays of (a) medium and (b) large GaAs dots after OMVPE growth. The scan area is 500 nm × 500 nm and height range is 40 nm.

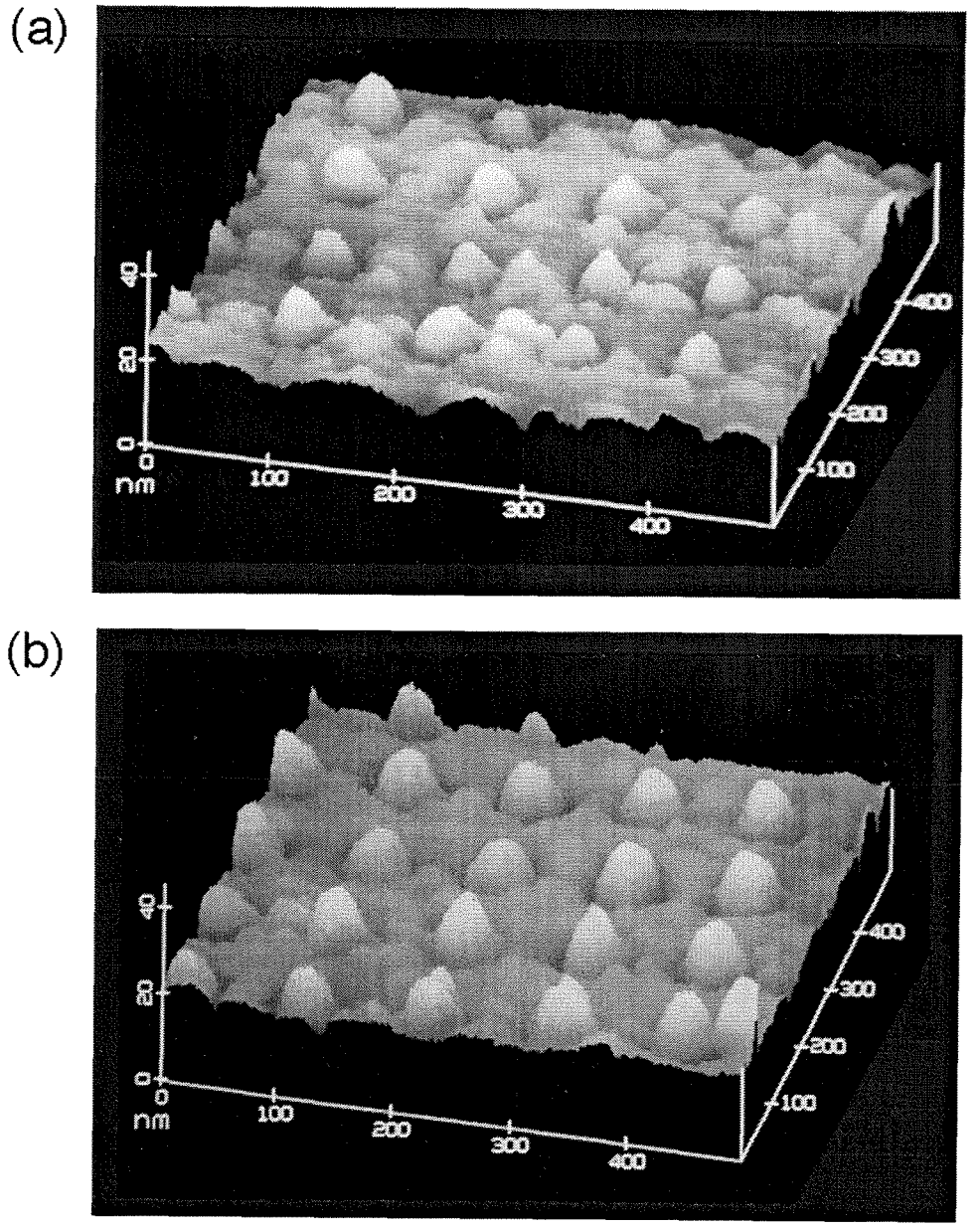

Figure 8.6: Atomic force micrographs in three-dimensional view of arrays of (a) small and (b) medium GaAs dots after removal of silicon nitride. The scan area is 500 nm × 500 nm and height range is 40 nm.

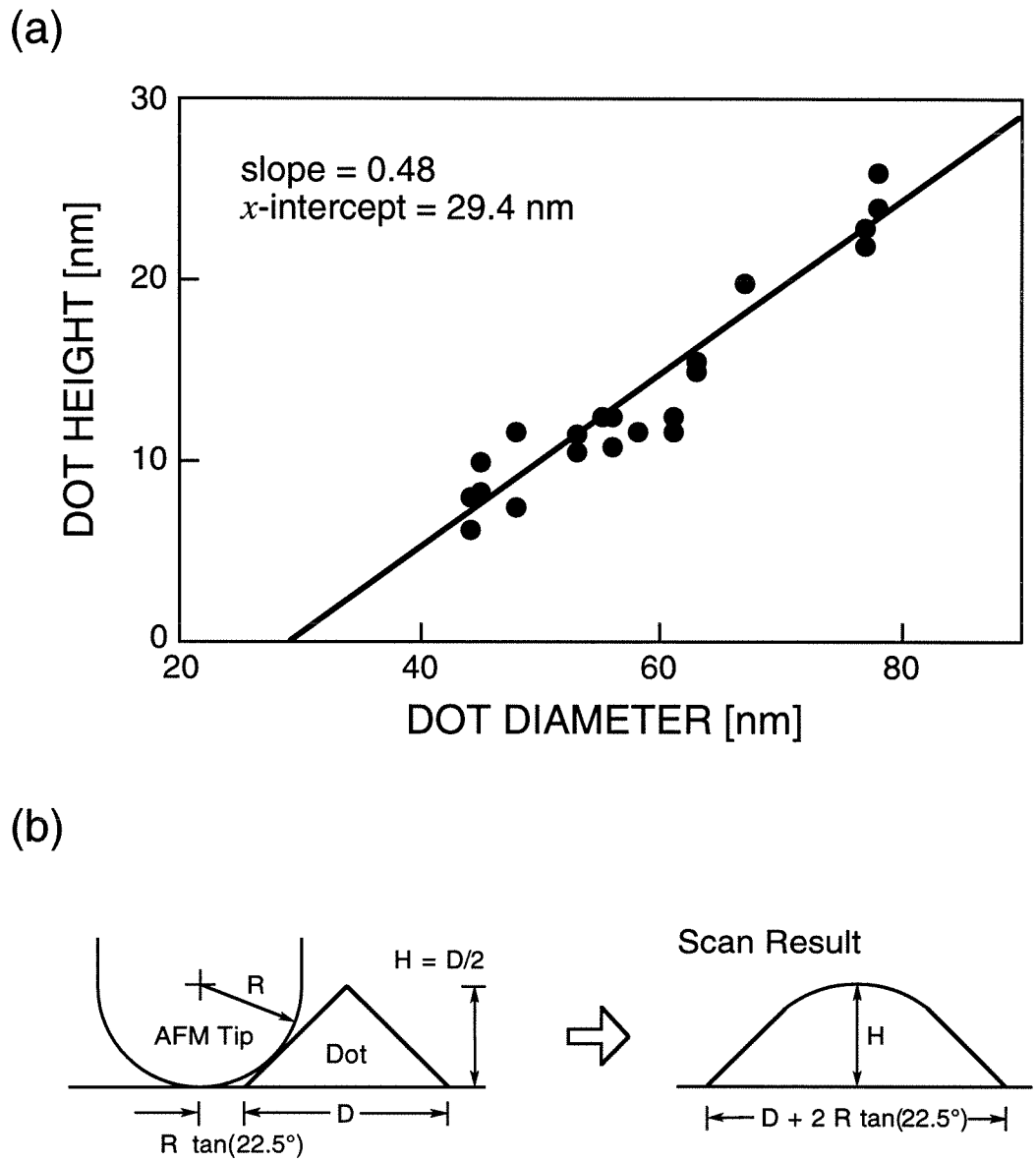

Figure 8.7: (a) Plot of GaAs dot height vs. base diameter measured after the silicon nitride removal. A best-fit line is also shown with an x-intercept of 29.4 nm and a slope of 0.48. (b) Idealized schematic illustrating the effect of finite radius of curvature R of the atomic force microscope probe tip on a dot structure with 45° facets and base width D.

diameter and 8–10 nm in height.

In conclusion, the formation of highly-uniform and densely-packed arrays of GaAs dots by selective epitaxy using diethylgallium-chloride and arsine has been demonstrated. Completely selective GaAs deposition within dielectric-mask openings is achieved at these small size-scales.

Bibliography

[1] H. Kroemer, "A proposed class of heterojunction lasers," *Proc. IEEE*, vol. 51, pp. 1782–1783, 1963.

[2] Zh. I. Alferov and R. F. Kazarinov, "Semiconductor laser with electrical pumping," U.S.S.R Patent 181737, 1963.

[3] Y. Arakawa, K. Vahala and A. Yariv, "Quantum noise and dynamics in quantum well and quantum wire lasers," *Appl. Phys. Lett.*, vol. 45, pp. 950–952, 1984.

[4] M. Asada, Y. Miyamoto and Y. Suematsu, "Gain and the threshold of 3-dimensional quantum-box lasers," *IEEE J. Quantum Electron.*, vol. QE-22, pp. 1915–1921, 1986.

[5] K. Kash, A. Scherer, J. M. Worlock, H. G. Craighead and M. C. Tamargo, "Optical spectroscopy of ultrasmall structures etched from quantum wells," *Appl. Phys. Lett.*, vol. 49, pp. 1043–1045, 1986.

[6] H. Temkin, G. J. Dolan, M. B. Panish and S. N. G. Chu, "Low-temperature photoluminescence from InGaAs/InP quantum wires and boxes," *Appl. Phys. Lett.*, vol. 50, pp. 413–415, 1987.

[7] J. Cibert, P. M. Petroff, G. J. Dolan, S. J. Pearton, A. C. Gossard and J. H. English, "Optically detected carrier confinement to one and zero dimension in GaAs quantum well wires and boxes," *Appl. Phys. Lett.*, vol. 49, pp. 1275–1277, 1986.

[8] D. Leonard, M. Krishnamurthy, C. M. Reaves, S. P. Denbaars and P. M. Petroff, "Direct formation of quantum-sized dots from uniform coherent islands of InGaAs on GaAs-surfaces," *Appl. Phys. Lett.*, vol. 63, pp. 3203–3205, 1993.

[9] S. Raymond *et al.*, "State filling and time-resolved photoluminescence of excited-states in $In_xGa_{1-x}As/GaAs$ self-assembled quantum dots," *Phys. Rev. B*, vol. 54, pp. 11548–11554, 1996.

[10] J. A. Lebens, C. S. Tsai, K. J. Vahala and T. F. Kuech, "Application of selective epitaxy to fabrication of nanometer scale wire and dot structures," *Appl. Phys. Lett.*, vol. 56, pp. 2642–2644, 1990.

[11] Y. D. Galeuchet, H. Rothuizen and P. Roentgen, "In-situ buried GaInAs/InP quantum dot arrays by selective area metalorganic vapor-phase epitaxy," *Appl. Phys. Lett.*, vol. 58, pp. 2423–2425, 1991.

[12] Y. Nagamune, S. Tsukamoto, M. Nishioka and Y. Arakawa, "Growth-process and mechanism of nanometer-scale GaAs dot-structures using MOCVD selective growth," *J. Crystal Growth*, vol. 126, pp. 707–717, 1993.

[13] Charles S. Tsai, Robert B. Lee and Kerry J. Vahala, "Formation of highly-uniform and densely-packed arrays of GaAs dots by selective epitaxy," Materials Research Society Proceedings vol. 358, *Microcrystalline and Nanocrystalline Semiconductors*, pp. 969–974, 1994.

[14] G. B. Stringfellow, *Organometallic Vapor-Phase Epitaxy, Theory and Practice*, Academic Press, San Diego, 1989.

[15] T. F. Kuech, M. S. Goorsky, M. A. Tischler, A. Palevski, P. Solomon, R. Potemski, C. S. Tsai, J. A. Lebens and K. J. Vahala, "Selective epitaxy of GaAs, $Al_xGa_{1-x}As$ and $In_xGa_{1-x}As$," *J. Crystal Growth*, vol. 107, pp. 116–128, 1991.

[16] T. F. Kuech, M. A. Tischler and R. Potemski, "Selective epitaxy in the conventional metalorganic vapor-phase epitaxy of GaAs," *Appl. Phys. Lett.*, vol. 54, pp. 910–912, 1989.

Appendix A

Low-Noise Erbium-Doped Fiber Preamplifier

A.1 Optically Preamplified Receiver

Rare-earth ion doped fiber amplifiers became practical in the late 1980's with the improved technology for the fabrication of low-loss doped optical fibers [1]. Erbium-doped fiber amplifiers (EDFAs) have attracted the most attention because they operate near 1.55 μm, the wavelength region of lowest loss in a silica optical fiber. EDFAs have found many applications in fiber-optic communication systems. With excellent amplification characteristics, such as high gain, large bandwidth and low crosstalk, EDFAs have been applied as power amplifiers, in-line amplifiers and optical receiver preamplifiers. In this appendix, its use in the last application is discussed. Optical preamplification increases signal strength resulting in typically an order of magnitude improvement of the receiver sensitivity [2].

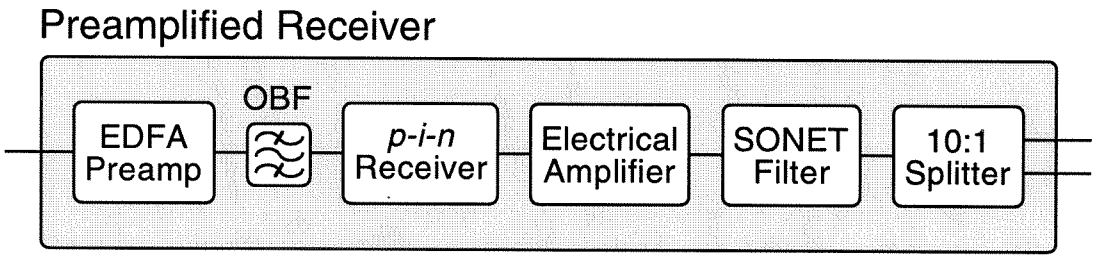

Figure A.1: Schematic of optically preamplified receiver.

A schematic of an optically preamplified receiver is shown in Fig. A.1. The critical elements that make up the preamplified receiver are: EDFA preamplifier, optical bandpass filter (OBF), *p-i-n* receiver, electrical amplifier and a SONET filter. The 10:1 splitter is used to allow for simultaneous measurement on two different instruments. The electrical components and the *p-i-n* receiver for optical-to-electrical conversion are commercially available components optimized for use in lightwave communication systems. The first component in the preamplified receiver, an EDFA preamplifier, was built in the laboratory. In this section, the figure of merit of the optical preamplifier is characterized and its impact on the bit-error-rate measurements are discussed.

A.1.1 Noise Figure of EDFAs

Amplifiers degrade the optical signal-to-noise ratio (SNR) of the signal due to the amplified spontaneous emission (ASE) added during the amplification process. The

SNR degradation is quantified by a parameter $F_{\rm n}$, referred to as the noise figure,

$$F_{\rm n} = \frac{({\rm SNR})_{\rm in}}{({\rm SNR})_{\rm out}}, \tag{A.1}$$

where SNR refers to the electrical SNR after the optical signal is detected using a photodetector. Although $F_{\rm n}$ depends on various parameters of the detector, to quantify the quality of the optical preamplifier, one often assumes an ideal detector limited only by shot noise.

Consider an amplifier with amplification G ($P_{\rm out} = GP_{\rm in}$). At the input, the SNR for a shot-noise limited signal is given by

$$({\rm SNR})_{\rm in} = \frac{\langle I \rangle^2}{\sigma_s^2} = \frac{(RP_{\rm in})^2}{2q(RP_{\rm in})\Delta f} = \frac{P_{\rm in}}{2h\nu\Delta f}, \tag{A.2}$$

where $\langle I \rangle = RP_{\rm in}$ is the average photocurrent, $R = q/h\nu$ is the unit quantum efficiency responsivity of a photodetector, $\sigma_s^2 = 2q(RP_{\rm in})\Delta f$ is the shot noise into the detector bandwidth Δf. For the amplified signal, one must take into account the spectral density of the added spontaneous emission noise $S_{\rm ASE} = n_{\rm sp}(G-1)h\nu$. The spontaneous-emission factor $n_{\rm sp}$ has a value ≥ 1 taking on the minimum value when the population inversion of the amplifier is complete (all atoms in the excited state). For the amplified signal, the beating of the ASE with the signal produces added current fluctuations at frequencies within the detector bandwidth ($\sigma_{\rm sig-ASE}$). The electrical noise power can be written as,

$$\sigma^2 = \sigma_{\rm s}^2 + \sigma_{\rm sig-ASE}^2 = 2q(RGP_{\rm in})\Delta f + 4(RGP_{\rm in})(RS_{\rm ASE})\Delta f. \tag{A.3}$$

The SNR of the amplified signal, for $G \gg 1$, is then given by

$$(\mathrm{SNR})_{\mathrm{out}} = \frac{\langle I \rangle^2}{\sigma^2} = \frac{(RGP_{\mathrm{in}})^2}{\sigma^2} \approx \frac{GP_{\mathrm{in}}}{4S_{\mathrm{ASE}}\Delta f}. \tag{A.4}$$

The noise figure can now be obtained by substituting in Eqns. A.2 and A.4 into the definition of noise figure. With a final substitution for S_{ASE}, we obtain

$$F_{\mathrm{n}} = 2n_{\mathrm{sp}}(G-1)/G \approx 2n_{\mathrm{sp}}. \tag{A.5}$$

This equation shows that even for an ideal amplifier ($n_{\mathrm{sp}} = 1$), the degradation factor of the SNR by amplification is 2 (or 3 dB). For application in optical communication systems, an optical amplifier with as low an F_{n} as possible is desired. Typically F_{n} can be as large as 6–8 dB, however, with proper design, a value near the theoretical limit can be achieved.

A.1.2 Bit-Error-Rate and Receiver Sensitivity

For a digital communication system, the overall system performance is quantified by the bit-error-rate (BER). The probability of error at the decision circuit is determined by the amount of fluctuation in the detected current around the average values I_1 and I_0 corresponding to a '1' or a '0' in the bit stream. The quality of different optical receiver systems can be compared using what is commonly referred to as the receiver sensitivity. A receiver is said to be more sensitive if it is able to achieve the same BER performance with less optical power. The following three cases are of interest: 1. quantum limited detection, 2. thermal-noise limited detection and 3. optically preamplified detection.

For a truly shot-noise limited detection involving only a very small number of photons and electrons, the receiver sensitivity or the average received power necessary for a BER $= 10^{-9}$ is given by [2][4]

$$\bar{P}_{\text{rec}} = N_{\text{p}} h\nu B/2 \tag{A.6}$$

according to Poisson statistics where N_{p} is 20 photons and B is the bit-rate. At 10 Gb/s, $\bar{P}_{\text{rec}} = -48.9$ dBm. This is a theoretical quantum limit. More typically receivers are limited by thermal noise $\sigma_{\text{T}}^2 = (4k_B T/R_L)\Delta f$. Assuming σ_{T} to be the dominant noise source, the receiver sensitivity can be calculated from the following:

$$\begin{aligned} \text{BER} &= \frac{1}{2}\text{erfc}(Q/\sqrt{2}) \\ Q &= \frac{I_1 - I_0}{\sigma_1 + \sigma_0} = \frac{R\bar{P}_{\text{rec}}}{\sigma_{\text{T}}}. \end{aligned} \tag{A.7}$$

For a receiver consisting of a p-i-n receiver and the subsequent electrical amplification with $\sigma_{\text{T}} \sim 5 \times 10^{-11}\sqrt{\Delta f}$ and a bit-rate of 10 Gb/s, $\bar{P}_{\text{rec}} = -17.7$ dBm where the electrical bandwidth Δf is assumed to equal $B/2$.

For an optically preamplified receiver, the noise power can be written as $\sigma^2 = \sigma_{\text{T}}^2 + \sigma_{\text{s}}^2 + \sigma_{\text{sig-ASE}}^2 + \sigma_{\text{ASE-ASE}}^2 + \sigma_{\text{s-ASE}}^2$ where the noise sources are thermal noise, signal shot-noise, signal-ASE beating noise, ASE-ASE beating noise and ASE shot-noise. The two dominant terms are

$$\begin{aligned} \sigma_{\text{sig-ASE}}^2 &= 2(qG)^2 F_{\text{n}} P_1 \Delta f/h\nu \\ \sigma_{\text{ASE-ASE}}^2 &= (qGF_{\text{n}})^2 \Delta\nu_{\text{opt}} \Delta f \end{aligned} \tag{A.8}$$

where F_{n} is the noise figure of the optical preamplifier and $\Delta\nu_{\text{opt}}$ is the optical filter bandwidth at the output of the optical preamplifier to minimize the total ASE enter-

ing the detector. The noise currents for the '1' and the '0' bit are approximated by $\sigma_1 = (\sigma^2_{\text{sig-ASE}} + \sigma^2_{\text{ASE-ASE}})^{1/2}$ and $\sigma_0 = \sigma_{\text{ASE-ASE}}$. The receiver sensitivity is

$$\bar{P}_{\text{rec}} = h\nu F_{\text{n}} \Delta f \left[Q^2 + Q(2\,\Delta\nu_{\text{opt}}/B)^{1/2} \right]. \tag{A.9}$$

For values of $\Delta\nu_{\text{opt}}/B = 10$, $F_{\text{n}} = 4$ dB and $B = 10$ Gb/s, the receiver sensitivity $\bar{P}_{\text{rec}} = -40.0$ dBm, within 10 dB of the quantum limit. Thus using this technique improvements of 10–20 dB in the receiver sensitivity can be achieved over a thermal-noise limited receiver. In one experiment [5] a receiver sensitivity of -37.2 dBm was achieved at 10 Gb/s.

A.2 EDFA Preamplifier Used in the Experiment

It has been shown in the previous section how system performance can be significantly improved by the use of an optically preamplified receiver. For the BER measurements presented in this thesis, due to the small available optical powers of the wavelength converted signal, a preamplified receiver is essential. The optical preamplifier was constructed for this purpose.

The schematic of the low-noise two-stage EDFA is shown in Fig. A.2(a). The design is motivated by an effort to build a high performance amplifier using only one 980 nm pump laser with approximately 100 mW of available power. For this purpose, a two-stage single-pump design is used. The two stages are separated by an isolator at the midpoint. Two 980/1550 nm WDMs (WDM2 and WDM3) are used about the isolator to bypass the unabsorbed 980 nm light to the second stage. In the case of a

cascaded amplifier system, the noise figure is given by [6][7]

$$F_{\mathrm{n}}^{\mathrm{eff}} = F_{\mathrm{n1}} + \frac{F_{\mathrm{n2}}}{G_1}. \tag{A.10}$$

Therefore, with sufficiently high gain G_1 in the first stage, the impact of F_{n2} on the overall noise figure is minimized. Thus it is critical that the noise performance of the first stage is optimized. For this reason, forward 980 nm pumping is used in conjuction with a short 11 m segment of *AT&T HE-980* Erbium-doped fiber to maximize the inversion in the first stage. The gain of the first stage is ~15 dB sufficient to accommodate a higher noise figure in the second stage. Low-noise moderate amplification of the first stage is then followed by a 20 m second stage which effectively acts as a "power amplifier."

The gain and noise figure performances are summarized in Fig. A.2(b). The unsaturated gain ranges from 26 to 44 dB over the wavelengths 1530–1560 nm. The strong spectral dependence of the amplifier deserves a note in its application in a receiver system; the improvement that the optical preamplification provides varies depending on the wavelength of the signal, as observed in the experimental results presented in this thesis. In a commercial system, a gain-flattened amplifier, in which the spectral dependence of the gain is equalized, is preferred. A common technique for gain flattening is by use of a long-period fiber bragg grating [8][9]. Also shown in Fig. A.2(b) is the measured noise figure of the amplifier. The optical technique for measuring the noise figure is described in Ref. [10]. The noise figure is approximately 4 dB for the complete wavelength range. The saturated output power of the amplifier, which is limited simply by the total 980 nm pump power available, is +11.5 dBm over

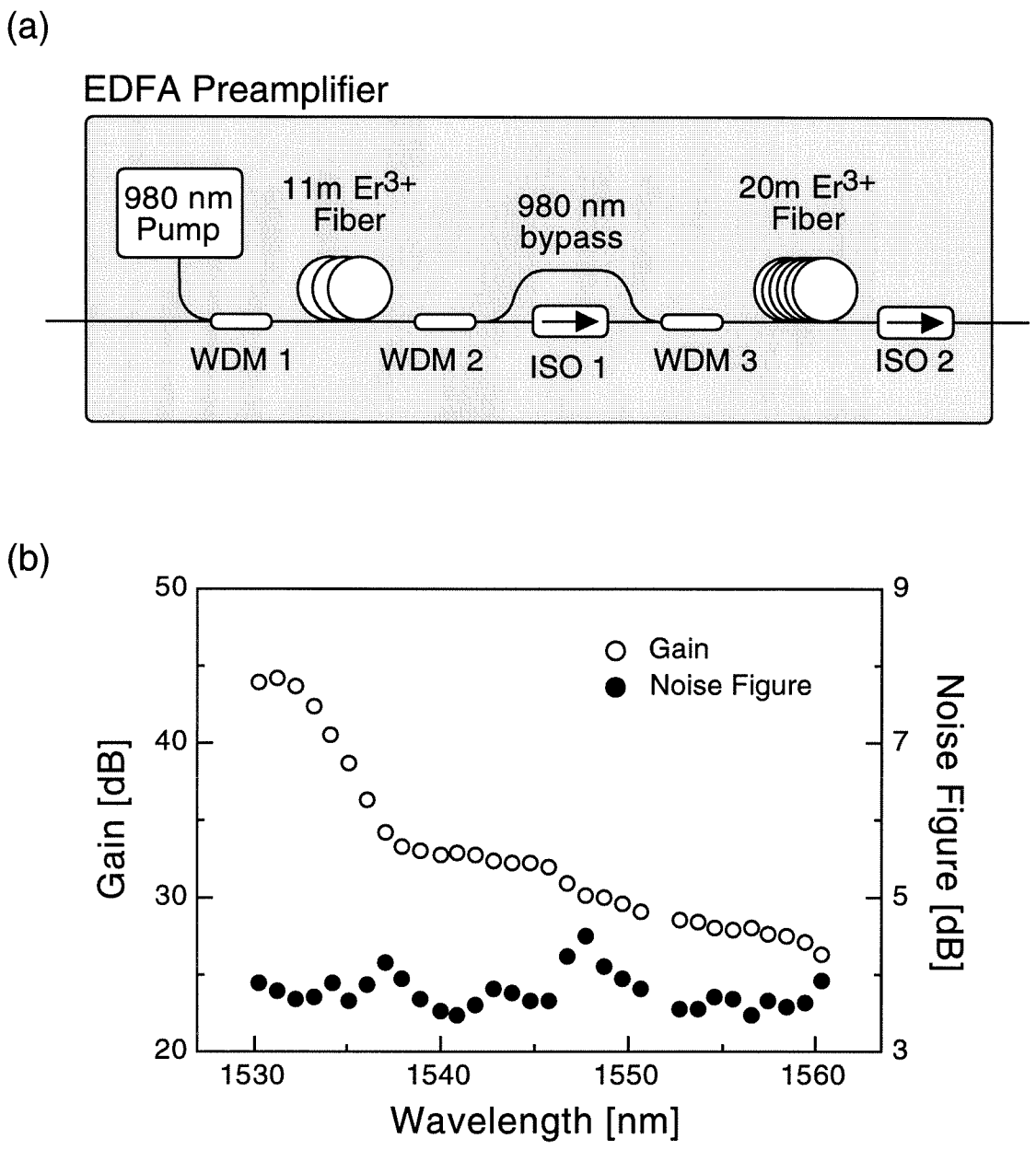

Figure A.2: (a) Schematic illustrating the detailed configuration of the low-noise, two-stage Erbium-doped fiber amplifier. (b) As a function of wavelength, the measured small signal gain and noise figure for an input power of approximately -35 dBm and 180 mA pump bias.

the complete 1530–1560 nm wavelength range.

Using this amplifier in the receiver system, a sensitivity as low as −35.2 dBm has been achieved at 10 Gb/s.

Bibliography

[1] S. B. Poole, D. N. Payne, R. J. Mears, M. E. Fermann and R. E. Laming, "Fabrication and characterization of low-loss optical fibers containing rare-earth ions," *J. Lightwave Technol.*, vol. 4, pp. 870–876, 1986.

[2] G. P. Agrawal, *Fiber-Optic Communication systems*, J. Wiley & Sons, New York, 1992.

[3] E. Desurvire, *Erbium Doped Fiber Amplifiers, Principles and Applications*, J. Wiley & Sons, New York, 1994.

[4] B. E. A. Saleh and M. Teich, *Fundamentals of Photonics*, chapter 11, J. Wiley & Sons, New York, 1991.

[5] T. Saito, Y. Sunohara, K. Fukagai, S. Ishikawa, N. Henmi, S. Fujita and Y. Aoki, "High receiver sensitivity at 10 Gb/s using an Er-doped fiber preamplifier pumped with a 0.98 μm laser diode," *IEEE Photon. Technol. Lett.*, vol. 3, pp. 551–553, 1991.

[6] Y. Yamamoto and T. Mukai, "Fundamentals of optical amplifiers," *Opt. Quantum Electron.*, vol. 21, pp. S1–S14, 1989.

[7] G. R. Walker, N. G. Walker, R. C. Steele, M. J. Creaner and M. C. Brain, "Erbium-doped fiber amplifier cascade for multichannel coherent optical-transmission," *J. Lightwave Technol.*, vol. 9, pp. 182–193, 1991.

[8] R. Kashyap, R. Wyatt and R. J. Campbell, "Wide-band gain flattened Erbium fiber amplifier using a photosensitive fiber blazed grating," *Electron. Lett.*, vol. 29, pp. 154–156, 1993.

[9] P. F. Wysocki, J. Judkins, R. Espindola, M. Andrejco, A. Vengsarkar and K. Walker, "Erbium-doped fiber amplifier flattened beyond 40 nm using long-period grating," *Optical Fiber Communication Conference 1997*, Dallas, Texas, post-deadline paper PD2.

[10] Hewlett-Packard Company, *EDFA Testing with the Interpolation Technique*, Product Note 71452-1, 1994.